Automatic segmentation of deep grey nuclei using a high-resolution 7T magnetic resonance imaging atlas-Quantification of T1 values in healthy volunteers

Gilles Brun, Benoit Testud, Olivier M Girard, Pierre Lehmann, Ludovic de Rochefort, Pierre Besson, Aurélien Massire, Ben Ridley, Nadine Girard, Maxime Guye, et al.

Automatic segmentation of Deep Grey Nuclei using a high-resolution 7T MRI Atlas - quantification of T1 values in healthy volunteers

Gilles Brun[1,2,3], Benoit Testud[1,2,3], Olivier M. Girard[1,2], Pierre Lehmann[1,2,3], Ludovic de Rochefort[1,2], Pierre Besson[1,2], Aurélien Massire[1,2], Ben Ridley[1,2,4], Nadine Girard[1,2,3], Maxime Guye[1,2], Jean-Philippe Ranjeva[1,2], Arnaud Le Troter[1,2,*]

[1]Aix Marseille Univ, CNRS, CRMBM, Marseille, France
[2]AP-HM, CHU Timone, Pôle d'Imagerie Médicale, CEMEREM, Marseille, France
[3]AP-HM, CHU Timone, Pôle d'Imagerie Médicale, Service de Neuroradiologie, Marseille, France.
[4]IRCCS Istituto delle Scienze Neurologiche di Bologna, Bologna, Italy

** Corresponding author*
e-mail: arnaud.le-troter@univ-amu.fr

Abstract

We present a new consensus atlas of deep grey nuclei obtained by shape-based averaging of manual segmentation of two experienced neuroradiologists and optimized from 7T MP2RAGE images acquired at $(0.6mm)^3$ in 60 healthy subjects. A group-wise normalization method was used to build a high-contrast and high-resolution T_1-weighted brain template $(0.5mm)^3$ using data from 30 out of the 60 controls. Delineation of 24 deep grey nuclei per hemisphere, including the claustrum and twelve thalamic nuclei, was then performed by two expert neuroradiologists and reviewed by a third neuroradiologist according to tissue contrast and external references based on the Morel atlas. Corresponding deep grey matter structures were also extracted from the Morel and CIT168 atlases. The data-derived, Morel and CIT168 atlases were all applied at the individual level using non-linear registration to fit the subject reference and to extract absolute mean quantitative T_1 values derived from the 3D-MP2RAGE volumes, after correction for residual B_1^+ biases.
Three metrics (The Dice and the volumetric similarity coefficients, and a novel Hausdorff distance) were used to estimate the inter-rater agreement of manual MRI segmentation and inter-atlas variability, and these metrics were measured to quantify biases due to image registration and their impact on the measurements of the quantitative T_1 values was highlighted.
This represents a fully-automated segmentation process permitting the extraction of unbiased normative T_1 values in a population of young healthy controls as a reference for characterizing subtle structural alterations of deep grey nuclei relevant to a range of neurological diseases.

Keywords
Ultra-high field; 7Tesla; MP2RAGE; Brain, Template; Shape-Based Averaging, Consensus-Atlas; Thalamic Nuclei; Deep Grey Nuclei; T_1 relaxometry.

Highlights

- Creation of an ultra-high resolution T_1-weighted MRI brain template at 7T (resolution $(0.5mm)^3$).
- Creation of a 3D atlas of deep grey nuclei (DGN) with thalamic nuclei segmentation into 12 parcels per hemisphere.
- Absolute T_1 values derived from B_1^+ corrected 3D-MP2RAGE are different between thalamic nuclei, and dependent on sex, age and brain hemisphere.
- Normative unbiased absolute T_1 values will help to characterize subtle DGN alteration in neurodegenerative diseases

This paper has been accepted for publication in European Journal of Neuroscience (the "Journal") published by John Wiley & Sons Ltd ("Wiley"):
Brun, G., Testud, B., Girard, O. M., Lehmann, P., de Rochefort, L., Besson, P., Massire, A., Ridley, B., Girard, N., Guye, M., Ranjeva, J.-P., & Le Troter, A. (2022). Automatic segmentation of deep grey nuclei using a high-resolution 7T magnetic resonance imaging atlas—Quantification of T1 values in healthy volunteers. European Journal of Neuroscience, 1–23. https://doi.org/10.1111/ejn.15575

Introduction

Direct visualization of the substructures in deep grey matter nuclei (DGN) is extremely challenging even with high-resolution MRI. The use of stereotactic atlases to determine DGN locations is the usual solution. However, most atlases fail to include certain small brain structures: the claustrum in particular, as well as some DGN and thalamic nuclei [Bazin and Pham, 2008]. Among DGN, the thalamus represents one of the most complex structures in the central nervous system [Ide et al., 2015], widely considered to constitute a "relay hub" with a range of motor, sensory and integrative functions [Hwang et al., 2017]. It is a large and deeply situated structure of the diencephalon, consisting of an oblique ovoid mass of grey matter located laterally to the third ventricle and medially to the internal capsule. Its complex anatomy is characterized by 31 nuclei involved in a wide range of behaviors including sleep-wake cycles, pain modulation and visual attention. These substructures are characterized by their afferent and efferent cortical projections and each nucleus is identified histologically by its cytoarchitecture [Jones, E.G., 2007; Morel et al., 1997]. This complexity has made the human thalamus a particular target of - and a challenge for - detailed imaging studies. Though inhomogeneous at the histological level [Toga et al., 2006], the thalamus appears homogenous in conventional MRI due to limited spatial resolution and concurrent partial volume effects [Bonnier et al., 2016]. Usually, indirect depiction of nuclei is performed based on stereotactic atlases [Talairach, J., 1957] with registration of the patient's MRI in a common neuroanatomical space. However, the direct identification of thalamic nuclei by MRI in individual patients would be of major interest for clinical and/or cognitive neuroscience research. Several methods have been used to enhance contrast between thalamic subregions including inversion recovery imaging [Magnotta et al., 2000; Sudhyadhom et al., 2009], high-resolution magnetization transfer imaging [Gringel et al., 2009], susceptibility-weighted imaging and quantitative susceptibility mapping (QSM) sensitive to in iron content [Abosch et al., 2010; Deistung et al., 2013] or by analyzing the intensity distribution within MPRAGE images [Bender et al., 2011; Tourdias et al., 2014].

Additionally, various post-processing and analysis methods have been applied to produce putative segmentations reflecting the microstructure of thalamic substructures: clustering approaches on quantitative T_1 and T_2 relaxation times [Traynor et al., 2011], thalamocortical connectivity-based segmentation derived from probabilistic tractography using Diffusion Tensor Imaging (DTI)[Behrens et al., 2003; Johansen-Berg et al., 2005; Traynor et al., 2010; Jakab et al., 2012; Lambert et al., 2017], and the orientation diffusion function (ODF) derived from high angle resolution Diffusion Weighted Imaging (DWI) [Battistella et al., 2017]. Furthermore, k-means clustering [Wiegell et al., 2003], and super-resolution track-density imaging have been shown to provide improved identification of thalamic nuclei [Calamante et al., 2013], permitting semi-automatic segmentation of the thalamus based on the fuzzy connectedness framework [Yang et al., 2015]. MRI has also been used in the construction of digital three-dimensional thalamic atlases based on histological sections [Niemann et al., 2000; Chakravarty et al., 2006; Yelnik et al., 2007; Krauth et al., 2010; Iglesias et al., 2018], with one post-mortem atlas based on 4.7T MR images identifying 31 substructures within the thalamus [Lemaire et al., 2010]. In line with these approaches, the electronic version [Krauth et al., 2010] of the Morel atlas [Morel, 2007], referred to as the e-Morel atlas here, has been proposed as a means of generating individualized thalamus target maps using non-linear matching of atlas data to the MNI152 space, and was recently compared by [Iglesias et al., 2018] who defined a probabilistic atlas composed of twenty-six thalamic nuclei, derived from six manual segmentations of ex-vivo images, and validated on thirty-nine in-vivo MPRAGE T_1 images acquired at 3T.

With the emergence of ultra-high field MRI ($B_0 \geq 7T$), substantially improved accuracy and spatial resolution have both become possible within clinically compatible scan times [Nowogrodzki, 2018], accompanied by improvement in signal- and contrast-to-noise ratios (SNR and CNR, respectively) and reduced partial volume effects. Substructures invisible at lower field strengths have already been shown amenable to *in-vivo* assessment at 7T, including delineation of the stripe of Gennari [Zeineh et al., 2014; Federau and Gallichan, 2016], depiction of subtle changes in morphometry in various pathologies [Eapen et al., 2011; Planche et al., 2019], and improved segmentation of the DGN and thalamus into subterritories based on functional connectivity [Lenglet et al., 2012].

Authors have recently proposed different high resolution multimodal templates of the human brain by Symmetric Group-wise Normalization (SyGN)[Avants et al., 2010] derived from Human Connectome Project structural MRI data. The authors define a subcortical atlas which covers the principal nuclei (included amygdala nuclei [Tyszka and Pauli, 2016], DGN [Pauli et al., 2018], hypothalamic nuclei [Neudorfer et al., 2020] with the exception of the thalamic nuclei.

Concerning the thalamic nuclei, Su and coworkers [Su et al., 2019] have proposed an automated multi-atlas approach (THOMAS's algorithm) for the segmentation and volume quantification of thalamic nuclei derived from white-matter-nulled MP-RAGE images acquired at 7T, a method which has the potential to contribute significantly to the understanding of disease progression in Alzheimer's disease, Parkinson's disease (PD), multiple sclerosis, and other pathologies. More recently, 7T MRI was also used to locate the ventro-intermediate nucleus using a multi-atlas segmentation method applied to susceptibility weighted images [Najdenovska et al., 2019].

Other high resolution approaches such as MP2RAGE [Marques et al., 2010] or MP2RAGEME [Caan et al., 2019] sequences have provided enhanced contrast based on quantitative relaxometry and susceptibility values for the characterization of grey matter structures. Datta et al. [Datta et al., 2020] have very recently adapted THOMAS's algorithm to automatically segment twelve thalamic nuclei from MP2RAGE images, and have demonstrated a comparable efficiency obtained with the dedicated white-matter-nulled MP-RAGE images, with results on eight healthy volunteers and five pediatric-onset multiple sclerosis.

Recently, [Corona et al., 2019] proposed an optimized multi-contrast segmentation algorithm that exploits the full potential of T_1, T_2* weighted and QSM contrast differences in the three major thalamic subnuclear groups, and highlighted biases in the Morel atlas based segmentation in these large region. In this optimized method, regions of interest are accurately defined in template space and approximated in single subjects with spatial regularization to increase the robustness of the approach.

In the current study, we aimed to take advantage of the MP2RAGE contrast and the high-resolution available at 7T in order to propose a new DGN atlas via the construction of an ultra-high-resolution T_1-weighted template focused on the thalamus and basal ganglia. This new atlas is obtained by a shape-based averaging fusion [Rohlfing and Maurer, 2007] of two atlases made separately by two expert neuroradiologists, following an accurate and consensual delineation process in the template space. We further aimed to validate the template registration and automatic segmentation processes in a separate validation sample that is used in the construction of the template/atlas. Finally, after automatic segmentation of the DGN, we performed quantitative analyses of unbiased T_1 values to study variations of tissue according to age, sex and brain hemisphere, and provide a normative reference in a young population of subjects for characterizing structural alterations of subtle structural alterations of the DGN relevant to a range of neurological diseases.

Materials and Methods

Participants

Sixty young healthy volunteers (30 males / 30 females) without psychiatric or neurological pathology were included and scanned at 7T. Inclusion criteria were age (18-65 years) and good general health as established via a detailed clinical history. Exclusion criteria were pregnancy, dental fillings, tattoos and implants.

Participants provided informed consent in compliance with the ethical requirements of the Declaration of Helsinki and the protocol was approved by the Local Human Research Ethics Committee (Comité de Protection des Personnes sud Méditerranée 2).

From all these subjects, two homogeneous groups (in age and sex) were defined for the construction and validation of our method (Table 1). Data from the whole 7TAMI dataset (Fig1 a) of controls were used for subsequent analyses.

Table 1: Demographic features (Age, Sex) for the thirty subjects used for the 7TAMIbrain$_{T1w_30}$ template construction and the remaining thirty subjects for the atlas validation.

		Template construction (N=30)	Atlas Validation (N=30)	Total (N=60)
Age	Mean±SD (Min-Max)	23.3±2.47 years (19-32)	25.0±3.7 years (20-45)	24.2±3.2 years (19-45)
Sex (%)	Male	14 (46.7%)	16 (53.3%)	30 (50%)
	Female	16 (53.3%)	14 (46.7%)	30 (50%)

Image acquisition

All data were acquired on a 7 Tesla MRI system (Magnetom Step 2 investigational device, Siemens Healthineers, Erlangen, Germany) using a 1Tx/32Rx head coil (Nova Medical, Inc., Wilmington, MA USA).

After an automatic B_0 shimming procedure, a whole brain B_1^+ map was acquired using a spin-echo based sequence by assessing the ratio of consecutive spin and stimulated echoes (WIP#658, Siemens Healthineers). Then, a whole brain three-dimensional (3D) Magnetization Prepared with two Rapid Acquisition Gradient Echoes sequence (MP2RAGE) was acquired [Marques et al., 2010]. MP2RAGE–acquisition parameters were: TA = 10.12 min; TR= 5000 ms ; TE=3.13 ms ; inversion times TI_1/TI_2 = 900/2750 ms ; flip angles α_1/α_2 = 6°/5° ; Acceleration factor GRAPPA=3; FOV = 240 mm ; voxel size = $(0.6\ mm)^3$ isotropic ; 256 sagittal partitions (partial Fourier 6/8). This sequence produces a T_1-weighted (T_1-w) image with a spatially normalized contrast with reduced reception field bias and provides a means of extracting a quantitative T_1 map that were corrected for the non-uniform B_1^+ excitation field according to the method described in [Massire et al., 2016]. Briefly, the analytical Bloch signal equations describing the MP2RAGE signal were computed for a large range of T_1 (from 100 ms to 4s) and B_1^+ (from 10% to 200% of nominal B_1^+) values to

generate a look-up table that relates the measured MP2RAGE signal in a given voxel and the corresponding B_1^+ with a unique T_1 value. The B_1^+ -corrected T_1 mapping reconstruction algorithm was implemented offline using Matlab (The MathWorks, Natick, MA, USA).

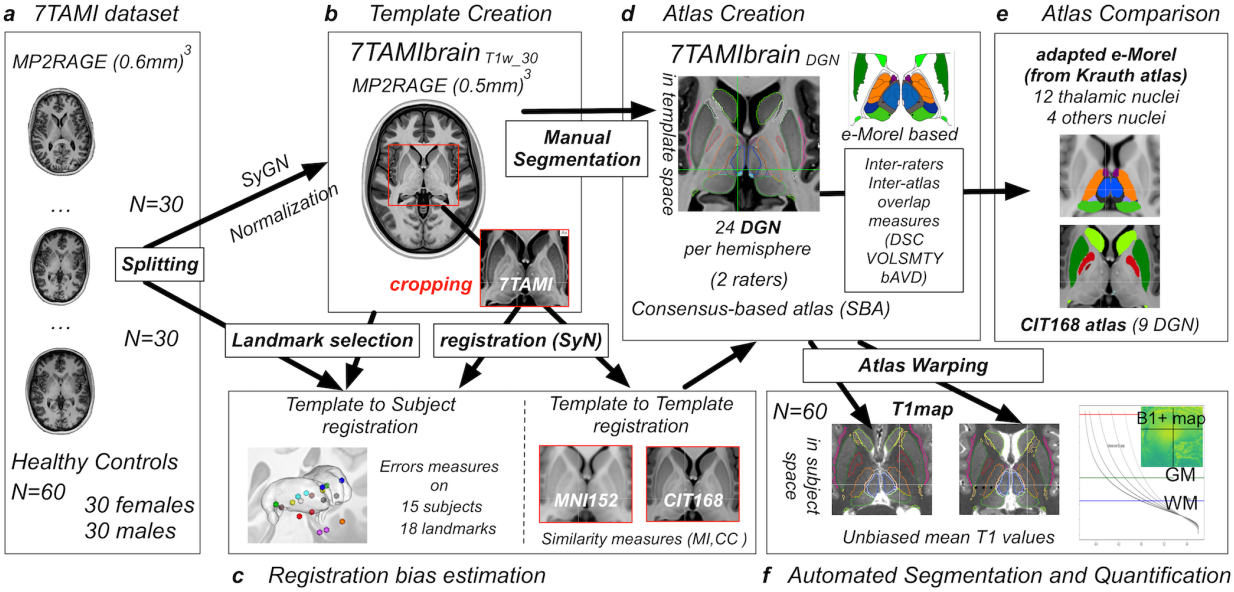

Fig1: Main steps in the post-processing pipeline - a) 7TAMI dataset short description (T_1-w axial views) - b) $7TAMIbrain_{T1w\_30}$ template creation - c) Registration bias estimation - d) $7TAMIbrain_{DGN}$ Atlas creation - e) Comparison of adapted e-Morel and CIT168 Atlases - f) Automated segmentation and unbiased T_1 quantification (T_1map axial views)

Template creation

A classical pipeline [Lau et al., 2020][Tyszka and Pauli, 2016] was used for the construction of a high-quality MRI brain template employing a combination of multi-scale average model construction and SyGN approaches [Avants et al., 2010; Avants et al., 2011]. Each T_1-w volume was resampled at isotropic voxel sizes of 0.5, 1, 2, 4 and 8 mm and blurred with Gaussian kernel sizes of 1, 2, 4, 8 and 16 (FWHM in voxel size). First, each iteration of non-linear registration by SyGN was estimated at the lowest resolution (8 mm). These images were then co-registered to create an 8 mm average-template after 4 iterations (Fig1 b). Oversampling by trilinear interpolation was performed to produce a 4 mm oversampled-template that became the target of the non-linear registration of each 4 mm down-sampled source image. The process was continued until the final resolution of $0.5mm^3$ was reached. Finally, the $7TAMIbrain_{T1w\_30}$ template (Fig1 b) was proposed in the normalized version via SyN registration in the standard MNI152 2009c nonlinear asymmetric space [Fonov et al., 2009], targeted on the T_1-w template upsampled at $(0.5\ mm)^3$.

Thus, we used the first included thirty subjects to build the $7TAMIbrain_{T1w\_30}$ template, and others thirty subjects to validate the registration process (Fig1 c).

Atlas creation

Two neuroradiologist raters R1 and R2 (G.B. and B.T.) performed manual delineation of the $7TAMIbrain_{T1w\_30}$ template bilaterally on each slice in the three planes (first pass on axial views, regularized on second and third passes in the sagittal and coronal views) using fsleyes software [McCarthy, Paul, 2020]. The boundaries were determined visually on the $7TAMIbrain_{T1w\_30}$ and assigned according to coordinates reported in the Morel's atlas [Morel et al., 1997]. Thus, two three-dimensional atlases of DGN ($7TAMIbrain_{R1}$ and $7TAMIbrain_{R2}$) were created including the following twenty-four structures in each hemisphere: twelve DGN (accumbens, caudate, claustrum, globus-pallidus-externus, globus-pallidus-internus, putamen, red-nucleus, sub-thalamic nucleus, substantia-nigra, caudatolenticar bridges, mammillothalamic tract (mtt), habenula) and twelve thalamic nuclei (lateral-geniculate, medial-geniculate, anterior, lateral, medial, posterior, lateral-posterior, central-lateral, centromedian, mediodorsal, pulvinar, pulvinar-anterior nuclei). All these thalamic nuclei were delineated on the template according to the nomenclature described in

the Morel Stereotactic Atlas of Human Thalamus [Morel et al., 1997]. A third neuroradiologist (PL) validated both segmentations of the structures without performing another manual delineation.

The consensus-based atlas (The 7TAMIbrain$_{DGN,}$ see Fig1 d) was generated by a shape-based averaging fusion algorithm [Rohlfing and Maurer, 2007] of the two rater atlases 7TAMIbrain$_{R1}$ and 7TAMIbrain$_{R2}$, following an internal consensual process of delineation described above. The main objective of this fusion was to restore spatial coherence, by correcting errors of continuity of the contours, which represent border effects that are difficult to avoid during manual delimitation in the three planes, at this spatial resolution.

To evaluate inter-expert variability and the integration of this variability in the construction of the consensus-based 7TAMIbrain$_{DGN}$ atlas three metrics were computed for each segmented region between the rater atlases 7TAMIbrain$_{R1}$, 7TAMIbrain$_{R2}$ and 7TAMIbrain$_{DGN}$. These included the Dice similarity coefficient (DSC), Volumetric similarity index defined as the ratio of the absolute volume difference divided by the sum of the compared volumes (referred to as VOLSMTY in [Taha and Hanbury, 2015], and equivalent to the VSI metric described in [Datta et al., 2020]), and the Balanced average Hausdorff distance (bAVD [Aydin et al., 2021] more suitable for rankings and quality assessment of segmentations than average Hausdorff distance).

For each of the 60 subjects SyN registration was used to warp the T_1-w image to the 7TAMIbrain$_{T1w_30}$ template. Then the individual inverse deformation fields were applied to the 7TAMIbrain$_{DGN}$ atlas. The SyN registration parameters were identical to those used during the last iteration of SyGN template creation [Avants et al., 2008]. The three neuroradiologists visually checked the sixty warped atlases for potential misalignments of the 7TAMIbrain$_{DGN}$ warped in individual subject spaces. Additionally, a quantitative assessment was performed after manual segmentation of eighteen anatomical regions of interest (habenula, junction anterior/lateral, junction lateral/pulvinar, mammillary body, medial geniculate nucleus, mammillothalamic tract, pulvinar peak, red nucleus for left and right hemispheres, anterior-commissure (ac) and posterior-commissure (pc)) in the native space of fifteen randomly selected individual subjects, and in the 7TAMIbrain$_{T1w_30}$ template. To evaluate the accuracy of the registration process, the 3D Euclidean distances (expressed in millimeters) between the centers of gravity of these eighteen regions projected into the 7TAMIbrain space and the corresponding regions segmented in the template were measured.

Post-processing

The MNI152 T_1-w MRI template (resolution $(0.5mm)^3$) associated with the e-Morel atlas was coregistered with the 7TAMIbrain$_{T1w_30}$ template and the corresponding spatial transform was applied to the 'adapted e-Morel' atlas. Non-linear warp was estimated by a standard three-stage process (rigid + affine + deformable b-spline SyN transformations), implemented in the ANTs Library using default parameters with the histogram matching option activated. Mutual Information (MI) was used for rigid and affine steps, and Cross-Correlation (CC) for the last BSplineSyN transformation (gradientStep=0.1, Correlation window radius = 4). The same registration process was performed with the MNI152 2009c (1mm space, nonlin asym version) [Fonov et al., 2009] associated to the CIT168 atlas. The corresponding spatial transform was applied to the 4D probabilistic CIT168 atlas thresholded at 0.5 and merged into one single 3D CIT168 atlas. Non-linear deformation was estimated by a standard three-stage process (rigid + affine + SyN transformations), with the same parameters described previously for the e-Morel atlas.

In order to estimate the projection biases related to the deformation fields induced by non-linear registration (template-to-subject registration, see Fig1 b,c), eighteen landmarks were positioned in the space of fifteen individual subjects, and in the template space by consensus of the two same neuroradiologists who segmented the 7TAMIbrain$_{DGN}$ (raters R1 and R2). Each landmark was selected by a single picking on image (size 2x2 voxels) and warped on the template space (using nearest-neighbor interpolation). The description of the landmark selection is as follows: the centers of the ac and pc, the center of mammillary body, the center of red-nucleus, the center of habenula, the center of medial geniculate nucleus, the pulvinar peak (i.e. in the axial plane passing through the center of the habenula, the peak of the anterior pulvinar nucleus which is clearly visible at the crossing between the medial and lateral group of thalamic nuclei), the lateral-pulvinar junction (outer edge of the thalamus at the intersection of the lateral nucleus group and the pulvinar on an axial plan through the center of the habenula), the mtt (at the junction with the internal medullary lamina in the coronal plane passing in the axis of the mammillothalamic tract), the lateral-anterior junction (outer edge of the thalamus at the intersection between the anterior nucleus group and the internal medullary lamina).

Template-to-template registrations (Fig1 b,c) were evaluated using Mattes mutual information (MI) and cross-correlation (CC) metrics before and after registrations on the associated templates. These metrics were estimated in the sub-region of the brain defined by a bounding box which covers all the labels of the 7TAMIbrain$_{DGN}$ atlas (CROP), and respectively in the targeted regions of interest respectively the thalamus for e-Morel atlas (THA) and the other grey nuclei for CIT168 atlas (DGN). The morphological differences among the adapted e-Morel atlas, CIT168 atlas

and the proposed 7TAMIbrain$_{DGN}$ atlas are estimated for each individual co-registered nucleus; DSC were performed to evaluate overlap mismatches.

Finally, we determined inter-subject and inter-atlas variability by comparing the distribution of mean T_1 and standard deviation values.

Overlap scores of parcels between the common thalamic nuclei (e-Morel atlas), DGN (CIT168 atlas), and the proposed 7TAMIbrain$_{DGN}$ atlas

The e-Morel atlas [Krauth et al., 2010] was modified to obtain comparable regions with respect to the 7TAMIbrain$_{DGN}$ atlas by merging subregions without visible boundaries on the 7TAMIbrain$_{T1w_30}$ template. Specifically, for each hemisphere, a total of thirty-four labels defining the entire set of thalamic nuclei in the e-Morel atlas were manually merged into twelve thalamic subregional labels as used in the 7TAMIbrain$_{DGN}$ atlas, as follows: lateral (VPM, VPLa, VPLp, VLa, VLpd, VLpv, VM, VAmc, VApc, VPI), mediodorsal (MDmc, MDpc), centromedian (CM), central-lateral (CL), medial (Pf, sPf, MV, CeM, Pv), medial-geniculate (MGN), lateral-geniculate (LGNmc, LGNpc), posterior (Po, SG, Li), lateral-posterior (LP), pulvinar (PuM, PuI, PuL), pulvinar anterior (PuA), anterior (AV, AM, AD, LD). We also delineated the habenula (Hb), mammillothalamic tract (mtt), red-nucleus (RN) and sub-thalamic nuclei (STh). In the following, this new atlas is referred to as the 'adapted e-Morel atlas'.

The CIT168 atlas [Pauli et al., 2018] was used to compare nine regions with respect to the 7TAMIbrain$_{DGN}$ atlas as follows: accumbens, caudate, globus-pallidus-externus, globus-pallidus-internus, habenula, putamen, red-nucleus, sub-thalamic, substantia-nigra (Pars Compacta and Pars Reticulata merged), and used to evaluate T_1 mean values for six others regions undefined in 7TAMIbrain$_{DGN}$ atlas as follows: extended-amygdala (EXA), hypothalamus (HTH), mammillary-nucleus (MN), parabrachial-pigmented-nucleus (PBP), ventral-pallidum (VeP) and ventral-tegmental-area (VTA).

DSC, VOLSMTY and bAVD were performed in the subject spaces for each common region, between 7TAMIbrain$_{DGN}$, CIT168 and adapted e-Morel atlases (Fig1 d,e).

Statistical analysis

Statistical analyses were performed with JMP statistical software, version 9.0.1 (SAS Institute). Mean T_1 values of each structure were evaluated via one-way analysis of variance (ANOVA). Post-hoc multiple comparison tests (Student and Tukey's HSD tests) were used to compare values among each nucleus and between hemispheres. Level of significance was defined as $p<0.05$, two-sided, corrected for multiple comparisons (Fig1 f).

The values obtained for the two different atlases were compared using a paired ANOVA, and direct comparisons corrected for multiple comparisons (Student and Tukey's HSD tests).

Results

Description of the 7TAMIbrain$_{T1w_30}$ template

Compared to single subjects, the final 7TAMIbrain$_{T1w_30}$ template allowed easier identification of nuclei of small size (RN, STh, SN) or with poor contrast on individual T_1-w images such as thalamic nuclei. The template provided excellent contrast in DGN (caudate (Cd), accumbens (Acb), and putamen (PuT)). Structures, such as the claustrum (Cl), internal accessory lamina (ial) and internal/external medullary lamina (iml, eml) of globus-pallidus externus and internus (GPe, GPi) were easily distinguished (Fig2). The fields of Forel, white matter areas of the subthalamus (fasciculus cerebellothalamicus (fct), fasciculus lenticularis (fl), fasciculus thalamicus (ft), ansa lenticularis (al), medial lemniscus (ml)), and Zona incerta (Zi) were clearly visible.

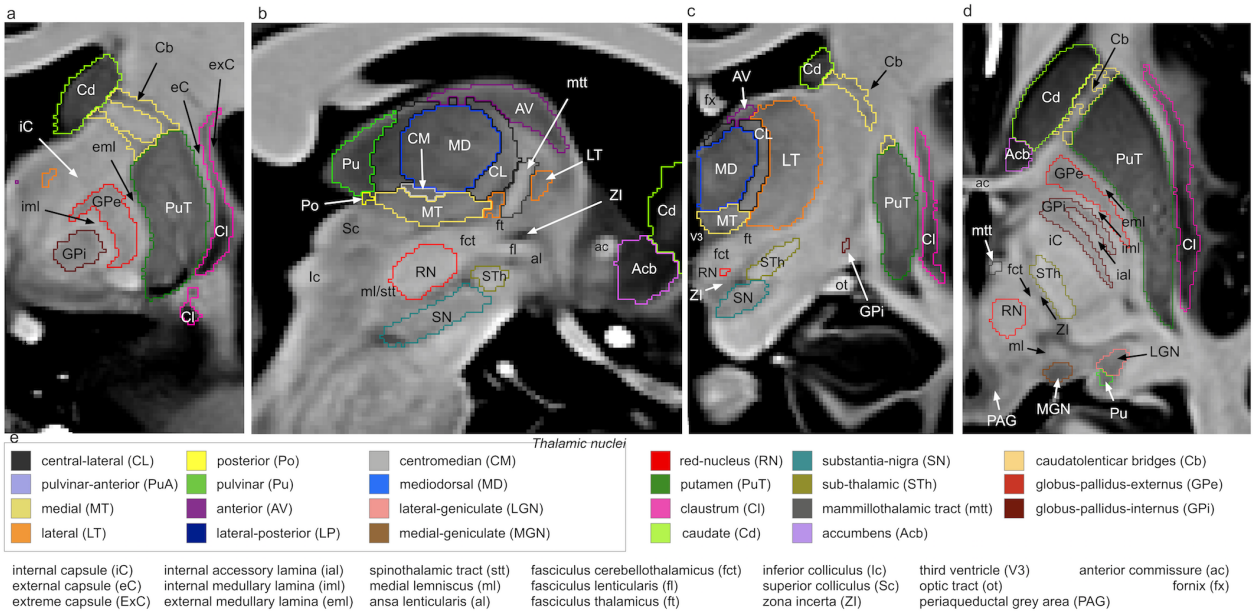

Fig2: Coronal, sagittal and axial cross-sections are displayed on the four slice displays to highlight accurate depiction and anatomical description of brain substructures, on the overlay of the 7TAMIbrain$_{T1w_30}$ template and the 7TAMIbrain$_{DGN}$ atlas.

a) claustrum and striatum nuclei (coronal view) - From internal to external: thalamus is separated from pallidum by the internal capsule (iC). pallidum is composed by the globus-pallidus-internus (GPi) and globus-pallidus-externus (GPe) separated by the internal medullary lamina (iml). The external medullary lamina (eml) is a thin white matter bundle between the GPe and the Putamen (PuT). Claustrum (Cl) is surrounded medially by the external capsule (eC) and laterally by the extreme capsule (exC).

b) thalamic and sub-thalamic nuclei, mtt (sagittal view) - The mtt links the thalamic anterior nuclei (AV) to the mammillary body. The mediodorsal (MD) is clearly visible above the thalamic medial nuclei (MT) (parafascicular and central medial nuclei). More hypointense, the pulvinar (Pu) is the most posterior nucleus. The red-nucleus (RN) can be distinguished from the Sn forward. Backward, the superior colliculus (Sc) and the inferior colliculus (Ic) form part of the tectal plate. Front (right), the anterior commissure (ac) is clearly identifiable.

c) thalamic and sub-thalamic nuclei (coronal view) – substantia-nigra (SN) and sub-thalamic nuclei (STh) are easily depicted. The MD of the thalamus borders the roof of the 3rd ventricle (V3). More laterally, the lateral nuclei of the thalamus (LT) are clearly visible with different intensities.

d) striatum, pallidum nuclei (axial view) - This cross-sectional slice shows the striatum composed of the putamen (PuT) and the caudate (Cd) linked by caudatolenticar bridges (Cb). The GPi is further partitioned along its caudal two-thirds by the internal accessory lamina (ial).

e) Legend: list of nuclei segmented in the 7TAMIbrain$_{DGN}$ and visible from at least one view

Inter-expert variability of individual and consensus-based 7TAMIbrain$_{DGN}$ atlas

The DSC, VOLSMTY and bAVD metrics between the two individual atlases delineated by the two neuroradiologists (G.B. (7TAMIbrain$_{R1}$). and B.T. (7TAMIbrain$_{R2}$)) and the resulting consensus-based atlas (7TAMIbrain$_{DGN}$) obtained by shape-based averaging fusion of both atlases, are reported for each nuclei in Table 2 (Thalamic nuclei values are separated from others DGN). For all nuclei (left and right sides averaged), the mean±stdev values between R1 and R2, DGN and R1, as well as DGN and R2 were respectively 0.74±0.10, 0.86±0.06, 0.87±0.05 for DSC, 0.91±0.07, 0.93±0.04, 0.95±0.04 for VOLSMTY, and 0.22±0.11, 0.11±0.07, 0.08±0.04 for bAVD (in mm). Merging the two expert delineations into a single segmentation led to an improvement in overlap mainly due to a spatial regularization of the contours of the nuclei.

Table 2 : Overlap Measures by nuclei, with Mean±stdev Dice similarity coefficient (DSC), Volumetric similarity coefficient (VOLSMTY) and balanced average Hausdorff distance (bAVD) estimated between the consensus-based atlas (7TAMIbrain$_{DGN}$), and the individual atlases segmented by two raters (7TAMIbrain$_{R1}$ and 7TAMIbrain$_{R2}$)

	DSC			**VOLSMTY**			**bAVD (in mm)**		
7TAMIbrain	**R1 vs R2**	**DGN vs R1**	**DGN vs R2**	**R1 vs R2**	**DGN vs R1**	**DGN vs R2**	**R1 vs R2**	**DGN vs R1**	**DGN vs R2**
DGN	0.78 ±0.08	0.89 ±0.05	0.88 ±0.04	0.91 ±0.08	0.94 ±0.03	0.93 ±0.05	0.17 ±0.08	0.09 ±0.06	0.07 ±0.03
Acb	0.84	0.93	0.91	0.97	0.98	0.97	0.11	0.04	0.05
Cd	0.91	0.96	0.95	0.99	0.98	0.98	0.08	0.05	0.02
CI	0.71	0.86	0.86	0.86	0.97	0.89	0.27	0.17	0.09
Cb	0.49	0.76	0.72	0.63	0.84	0.78	0.45	0.30	0.22
GPe	0.85	0.93	0.93	0.97	0.94	0.97	0.09	0.04	0.04
GPi	0.79	0.91	0.90	0.98	0.93	0.94	0.11	0.05	0.05
Hb	0.72	0.86	0.84	0.94	0.93	0.89	0.16	0.08	0.09
mtt	0.75	0.83	0.87	0.94	0.94	0.92	0.21	0.13	0.08
PuT	0.95	0.98	0.97	0.99	0.99	0.98	0.03	0.01	0.02
RN	0.78	0.87	0.91	0.82	0.88	0.94	0.18	0.07	0.05
SN	0.73	0.86	0.88	0.96	0.95	0.99	0.19	0.08	0.07
STh	0.79	0.92	0.87	0.86	0.98	0.88	0.11	0.04	0.07
Thalamus nuclei	0.70 ±0.11	0.83 ±0.08	0.85 ±0.05	0.90 ±0.06	0.92 ±0.04	0.96 ±0.02	0.27 ±0.12	0.13 ±0.07	0.09 ±0.03
AV	0.72	0.88	0.83	0.89	0.96	0.94	0.24	0.12	0.10
CL	0.66	0.82	0.85	0.81	0.84	0.97	0.30	0.12	0.09
CM	0.60	0.76	0.80	0.93	0.94	0.90	0.32	0.13	0.11
LGN	0.74	0.91	0.84	0.96	0.94	0.98	0.17	0.05	0.09
LP	0.61	0.78	0.81	0.87	0.90	0.97	0.40	0.20	0.12
LT	0.88	0.94	0.93	0.97	0.98	0.99	0.10	0.03	0.04
MD	0.88	0.92	0.95	0.95	0.97	0.99	0.08	0.04	0.03
MGN	0.72	0.84	0.88	0.81	0.87	0.94	0.23	0.10	0.06
MT	0.64	0.75	0.87	0.94	0.93	0.99	0.53	0.37	0.07
Po	0.50	0.72	0.73	0.75	0.79	0.95	0.40	0.22	0.16
Pu	0.91	0.95	0.95	0.98	0.98	0.97	0.06	0.03	0.02
PuA	0.55	0.72	0.77	0.95	0.93	0.98	0.40	0.15	0.14
All nuclei	0.74 ±0.10	0.86 ±0.06	0.87 ±0.05	0.91 ±0.07	0.93 ±0.04	0.95 ±0.04	0.22 ±0.11	0.11 ±0.07	0.08 ±0.04

The comparable increase (>0.1) of the DSC between the consensus-based atlas and the individual rater atlases shows the ability of the fusion method to reduce inter-expert variability, while maintaining spatial coherence.

Bias estimation for template-to-subject registration

The mean±stdev distance between centers of mass between template landmarks and warped landmarks of subjects of all regions of interest was 1.18±0.80 mm. Detailed values for each landmark are reported in Table 3.

Table 3: Error measures on anatomical landmarks, in the estimation of deformation by non-linear SyN registration between fifty individual subjects and the 7TAMIbrain$_{T1w_30}$ template computed on eighteen anatomical landmarks.

Landmarks	**Errors mean±stdev**	**(in mm)**
	Left Hemisphere	Right Hemisphere
ac	0.39±0.21	
pc	0.40±0.21	
Hb	0.66±0.30	0.91±0.27
anterior/lateral junction	1.08±0.55	1.31±0.69
lateral/pulvinar junction	2.16±0.76	2.09±1.07
mammillary body	0.65±0.20	0.54±0.19
MGN	1.24±0.40	1.12±0.51
mtt	1.03±0.45	0.78±0.29
pulvinar peak	1.70±0.62	1.90±0.90
RN	1.04±0.39	1.80±1.40
all regions	1.18±0.80	

In Fig3, all landmarks are represented in the 7TAMIbrain$_{T1w_30}$ space with a morphological dilation (sphere kernel 1.8 mm, radius of 3 voxels), and shows an accurate matching between the template landmarks and the projected subject's landmarks, to validate the registration in these regions of interest.

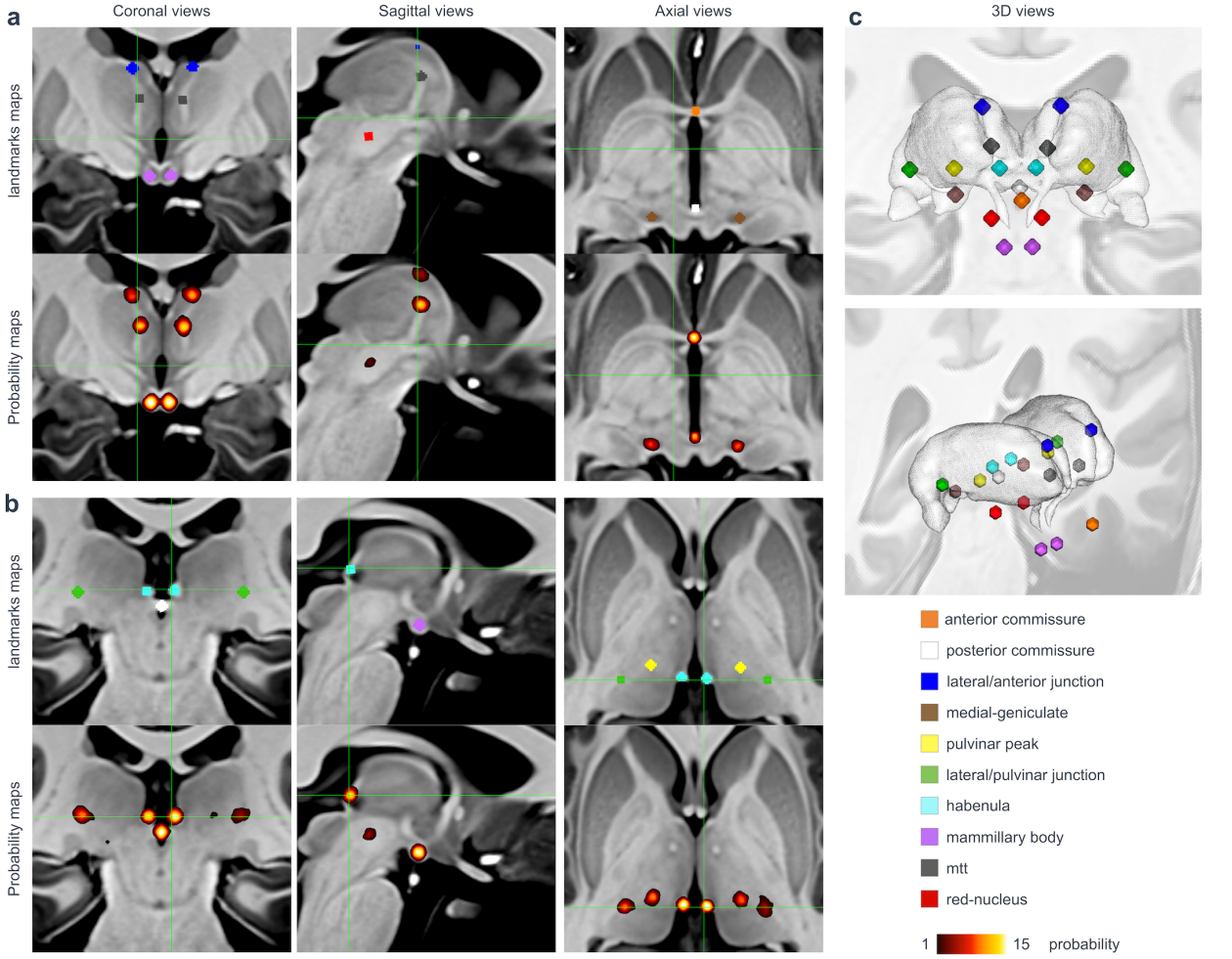

Fig3: Coronal, sagittal and axial, and 3D views of all landmarks. a) lateral/anterior junction, mtt, mammillary body, red-nucleus, anterior/posterior commissures, medial geniculate. b) lateral/pulvinar junction, habenula, mammillary body, pulvinar peak. The plain color maps representing template landmarks (first and third rows) and the hot-color probability maps corresponding to the sum of individual landmark maps warped and interpolated in the template space (second and fourth rows). c) 3D views and legend of landmarks showing a large cover of the thalamus and subthalamus.

Non-linear template-to-template registration

The two-step registration procedure including affine and non-linear transforms showed a large gain in the evaluation of similarity measures between templates (cross correlation and mutual information), especially after the non-linear registration.

In the bounding box including all DGN, the measures of similarity between the $7TAMIbrain_{T1w\_30}$ template and MNI152 T_1-weighted MRI template associated with the e-Morel atlas increased from 0.35 to 0.60 (+71%) for CC and from 0.63 to 0.92 (+46%) for MI, after nonlinear SyN registration. The similarity measures between these two templates led to a lower matching increase of labeled regions common to the two atlases from 0.29 to 0.50 (+72%) for CC, and from 0.30 to 0.38 (+26%) for MI in the thalamus, while CC rose from 0.45 to 0.51 (+13%) and MI from 0.33 to 0.44 (+33%) for the DGN. However, these measures indicate that the final match, after nonlinear registration between these two different templates, was still not optimal.

Similarly, the matching between the $7TAMIbrain_{T1w\_30}$ template and 'MNI152 2009c nonlin asym' template associated with the CIT168 atlas increased after the nonlinear SyN registration from CC values of 0.50 to 0.63 (+26%) and MI values of 0.81 to 1.01 (+25%). Thus, the better match of these two templates led to a matching increase of labeled regions common to the two atlases, with CC rising from 0.45 to 0.73 (+62%) and MI from 0.62 to 0.90 (+45%) for the DGN and CC rising from 0.63 to 0.68 (+8%) and MI from 0.60 to 0.63 (+5%) for the thalamus.

In the common regions to the three atlases (habenula, sub-thalamic nuclei, red nuclei), the similarities between 'MNI152 2009c nonlin asym' and $7TAMIbrain_{T1w\_30}$ templates are better than those estimated with e-Morel and $7TAMIbrain_{T1w\_30}$ templates, with respective values of 0.16 and 0.11 (+45%) for MI, 0.44 and 0.23 (+91%) for CC. These low MI and CC values may explain the poor overlap on the corresponding labels, which correspond with the low DSC values estimated in the subject spaces (ranging from 0.73 to 0.90 for CIT168 and 0.55 to 0.70 for e-Morel).

Table 4: Overlap Measures by nuclei, with Mean±stdev Dice similarity coefficient (DSC), Volumetric similarity coefficient (VOLSMTY) and balanced average Hausdorff distance (bAVD) estimated between the consensus-based atlas ($7TAMIbrain_{DGN}$), adapted electronic Morel Atlas (thalamic nuclei) and CIT168 atlas.

	DSC		**VOLSMTY**		**bAVD (in mm)**	
7TAMIbrain vs	**CIT168**	**Adapted e-Morel**	**CIT168**	**Adapted e-Morel**	**CIT168**	**Adapted e-Morel**
DGN	0.80±0.09	0.49±0.22	0.92±0.05	0.84±0.08	0.19±0.15	0.61±0.79
Acb	0.70±0.14		0.88±0.10		0.42±0.30	
Cd	0.89±0.01		0.94±0.01		0.11±0.01	
GPe	0.83±0.02		0.90±0.01		0.13±0.02	
GPi	0.75±0.01		0.91±0.01		0.21±0.07	
Hb	0.73±0.04	0.55±0.05	0.90±0.03	0.74±0.08	0.29±0.07	0.52±0.13
mtt		0.13±0.04		0.88±0.05		0.99±0.12
PuT	0.91±0.00		0.97±0.01		0.08±0.01	
RN	0.90±0.01	0.70±0.03	0.96±0.01	0.91±0.02	0.07±0.01	0.42±1.47
SN	0.72±0.01		0.88±0.01		0.29±0.03	
STh	0.78±0.02	0.59±0.04	0.96±0.02	0.83±0.06	0.15±0.01	0.49±0.36
Thalamus nuclei		0.53±0.20		0.70±0.20		1.29±2.49
AV		0.49±0.04		0.63±0.03		0.94±0.18
CL		0.56±0.02		0.97±0.02		0.41±0.03
CM		0.45±0.02		0.46±0.02		1.62±0.18
LGN		0.42±0.03		0.51±0.04		1.56±0.20
LP		0.62±0.08		0.72±0.05		0.64±0.31
LT		0.83±0.02		0.87±0.02		0.19±0.04
MD		0.83±0.02		0.91±0.01		0.14±0.03
MGN		0.17±0.05		0.51±0.04		4.20±4.27
MT		0.52±0.03		0.87±0.04		0.47±0.04
Po		0.44±0.03		0.52±0.03		1.33±0.15
Pu		0.76±0.05		0.96±0.01		0.26±0.07
PuA		0.24±0.09		0.44±0.03		3.67±6.02
All nuclei		0.62±0.22		0.80±0.18		0.78±1.82

Overlap Measures between 7TAMIbrain$_{DGN}$, adapted e-Morel Atlas and DGN (CIT168 atlas)

The mean±stdev DSC, VOLSMTY and bAVD between 7TAMIbrain$_{DGN}$ and adapted e-Morel atlas of all thalamic nuclei were respectively 0.53±0.20, 0.70±0.20, 1.29±2.49, and for other DGN between 7TAMIbrain$_{DGN}$ and CIT168 atlas were 0.80±0.09, 0.92±0.05, 0.19±0.15. For each nucleus and for all metrics, the values are detailed in Table 4.

Several differences between the three atlases and corresponding templates, in term of nuclei delineation and template contrasts, are clearly visible on Fig4.

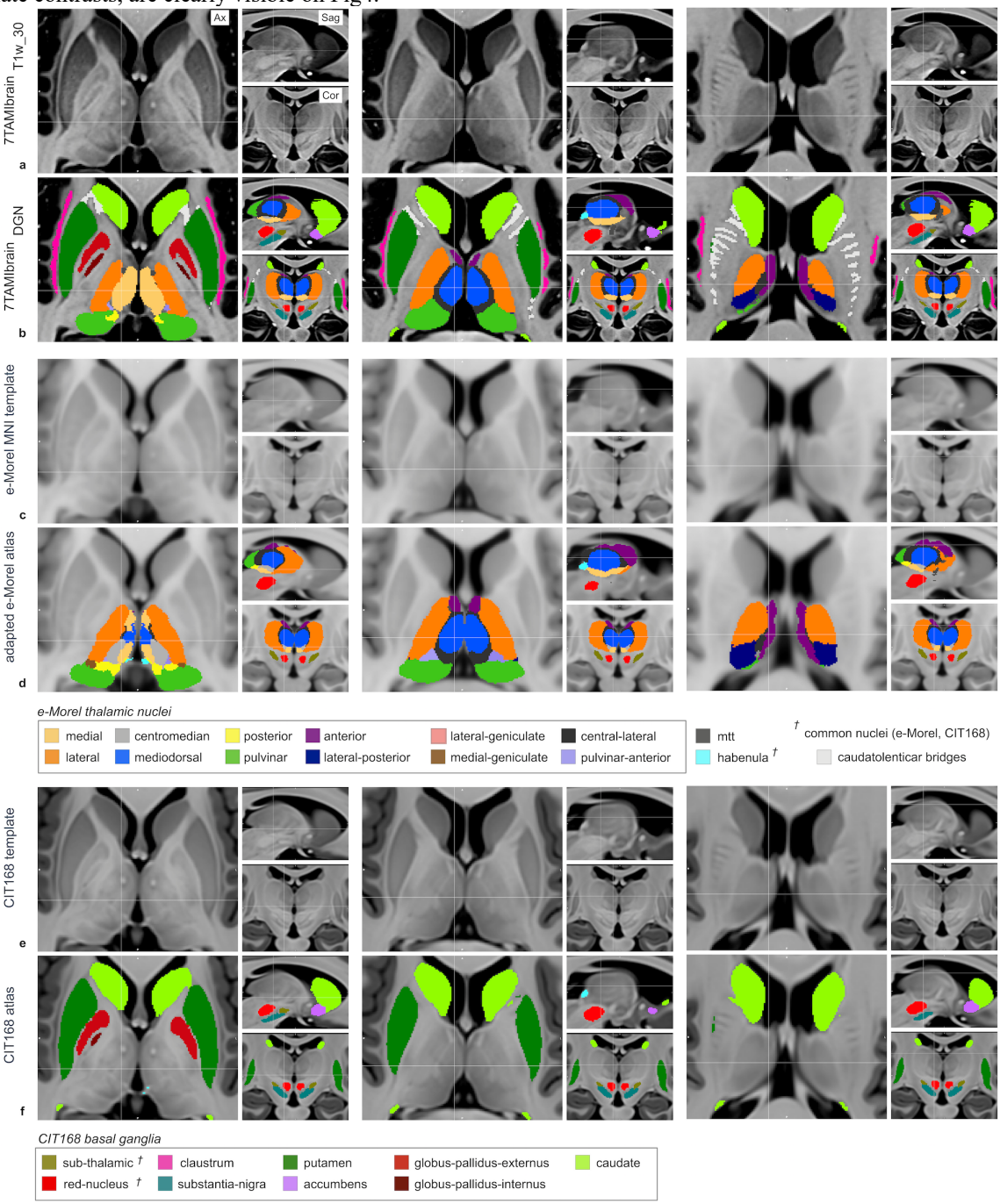

Fig4: Axial, sagittal and coronal views showing the results of the manual segmentation of 7TAMIbrain$_{DGN}$ atlas and the corresponding slices of the adapted e-Morel Atlas. a) 7TAMIbrain$_{T1w_30}$ views, b) 7TAMIbrain$_{DGN}$ views, c) Legend: list of nuclei segmented in the 7TAMIbrain$_{DGN}$ and adapted e-Morel atlas (common label are identified by a mark †) d) adapted e-Morel atlas corresponding to the 7TAMIbrain$_{DGN}$ e) MNI T_1-weighted template associated to e-Morel and co-registrered to the 7TAMIbrain$_{T1w_30}$ template

Mean T_1 values derived from the 7TAMIbrain$_{DGN}$, the e-Morel and the CIT168 atlases

Mean T_1 values of DGN and thalamic nuclei varied in the range of [1322ms-2003ms] for the 7TAMIbrain$_{DGN}$, [1330ms-2036ms] for the adapted e-Morel atlas and [1309ms-2019ms] for the CIT168 atlas. The correspondence of these values is illustrated via biplot representation in Fig5 a,d and boxplot representation in Fig5 b,e to highlight differences between the inter-subject distributions and ranking per nucleus in ascending order of mean T_1 values of 7TAMIbrain$_{DGN}$. The largest mismatches were observed for the habenula, mtt, red-nucleus and for thalamic nuclei (i.e. anterior, central-lateral, lateral-geniculate, medial, posterior, pulvinar, pulvinar-anterior) (Wilcoxon rank test $p < 0.00001$), showing longer T_1 values and larger variance (Table 5, Fig5 c,f) for the adapted e-Morel Atlas compared to the 7TAMIbrain$_{DGN}$. Mean T_1 values of lateral and medial geniculate were significantly longer for the 7TAMIbrain$_{DGN}$ but with comparable variances compared to the adapted e-Morel Atlas.

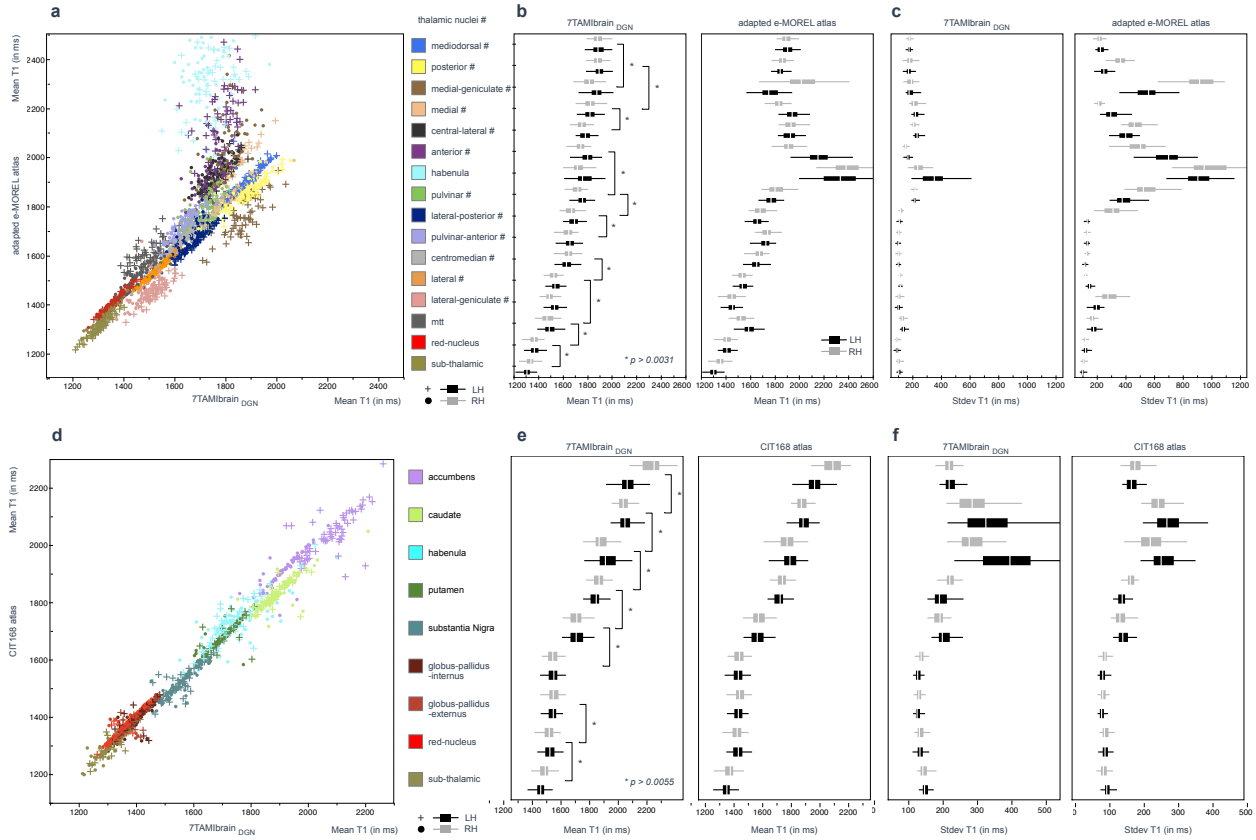

Fig5: biplot representations of mean T_1 values for each subject (N=60), of thalamic nuclei between 7TAMIbrain$_{DGN}$, the adapted e-Morel atlas (a) and the CIT168 atlas (d), respective boxplot representations between the inter-subject distributions and ranking per nucleus in ascending order of mean T_1 values (b and e), and corresponding stdev T_1 values (c and f).

* $p<0.05$ corrected for multiple comparisons ($p<0.0031$ for Morel atlas, $p<0.0055$ for CIT168 atlas)

No significant regional differences in T_1 values were found between the 30 subjects used to build the template and the 30 subjects used as validation sample (median uncorrected p value = 0.525; range [0.027-0.965] over the 48 regions, Wilcoxon rank tests).

Table 5: Comparison of T_1 values (Mean+SD in ms) of thalamic nuclei (adapted electronic Morel Atlas) and DGN (CIT168 atlas) derived from the 7TAMIbrain$_{DGN}$ atlas.

	Names	7TAMIbrain$_{DGN}$ (1)	Adapted e-Morel(2)	CIT168 (3)	Wilcoxon rank test 1 vs 2 / 1 vs 3 / 2 vs 3
other deep grey nuclei	Acb	2003±110		1977±95	0.0939
	Cd	1895±58		1831±49	< 0.0001*
	Cl	1614±45			0.1675
	Cb	1442±41			
	GPe	1393±39		1384±39	0.0546
	GPi	1396±41		1383±41	0.0239
	Hb	1787±163	1733±78	1733±78	< 0.0001* 0.1576 < 0.0001*
	mtt	1486±52	1560±63		< 0.0001*
	PuT	1701±45		1676±44	< 0.0001*
	RN	1369±42	1410±43	1374±43	< 0.0001* 0.3082 < 0.0001*
	SN	1561±56		1520±53	< 0.0001*
	STh	1322±44	1330±50	1309±45	0.2896 0.0223 0.0015*
	EXA			2019±81	
	HTH			1970±63	
	MN			1822±92	
	PBP			1576±54	
	VeP			1510±60	
	VTA			1616±61	
thalamic nuclei	AV	1769±56	2036±151		< 0.0001*
	CL	1770±48	1931±57		< 0.0001*
	CM	1638±48	1661±49		0.0004*
	LGN	1511±47	1453±51		< 0.0001*
	LP	1680±50	1670±53		0.1289
	LT	1533±41	1538±40		0.3373
	MD	1887±50	1901±51		0.0524
	MGN	1843±72	1897±188		0.2057
	MT	1829±63	1899±102		< 0.0001*
	Po	1886±65	1851±60		< 0.0001*
	Pu	1738±50	1795±64		< 0.0001*
	PuA	1652±49	1729±51		< 0.0001*

* $p<0.05$ corrected for multiple comparisons ($p<0.0023$).

The non-linear deformations applied to the 7TAMIbrain$_{DGN}$ atlas to extract the quantitative T_1 values of the individual subjects allowed an appropriate delineation of the structures without the need for manual correction by the radiologists on the warped atlases (Fig6).

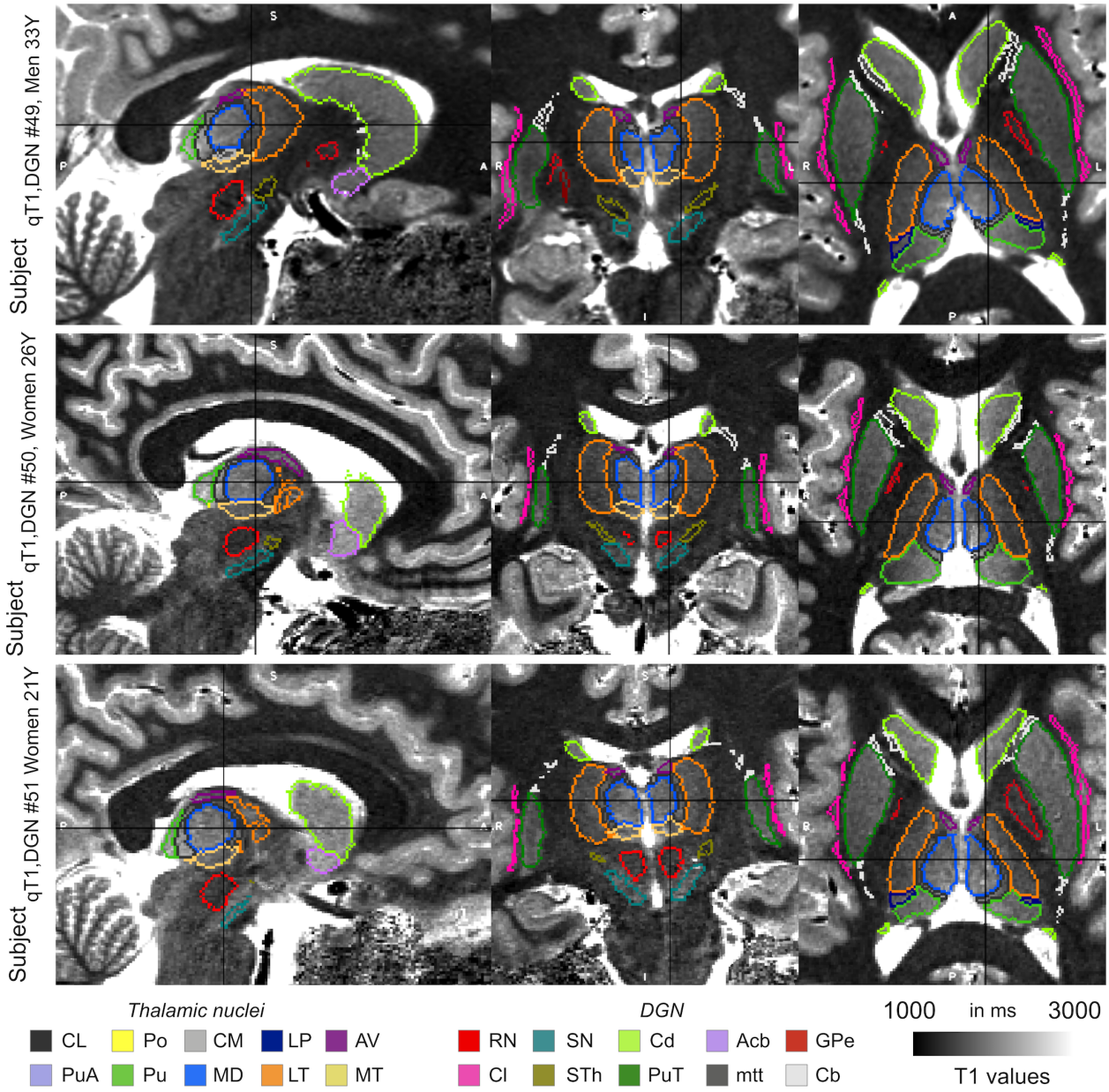

Fig6: Automatic segmentation results for three individual T_1 maps randomly selected using non-linear SyN deformation of 7TAMIbrain$_{DGN}$

Influence of hemisphere, sex and age on DGN T_1 values

Using the whole database T_1 values as the dependent variable, an ANOVA including age, sex, hemisphere, subject and regions as variables of interest revealed a significant global effect of the whole model ($F=8.83$; $p<0.0001$), with significant effects of brain hemisphere ($F=22.88$; $p<0.0001$), region ($F=22.41$; $p<0.0001$), age ($F=10.01$; $p<0.0016$), and sex ($F=7.36$; $p<0.0067$) without significant effect of subject ($F=0.64$, $p=0.4227$).

Significant longer T_1 values (corrected for multiple comparisons $p<0.0008$) were observed in the right hemisphere compared to the left, within accumbens (mean T_1 right Acb=2088ms+76ms, mean T_1 left Acb=1917ms+60ms, $p<0.0001$) and the sub-thalamic nuclei (mean T_1 right STh=1335ms+44ms, mean T_1 left STh=1309ms+41ms, $p=0.0007$). In contrast, within the thalamus, longer T_1 values were observed in the left hemisphere compared to the right especially for the anterior thalamic nucleus (mean T_1 left AV=1794ms+57ms, mean T_1 right A=1744ms+44ms, $p<0.0001$), the lateral geniculate (mean T_1 left LGN = 1533ms+42ms, mean T_1 right LGN 1488ms+41ms, $p<0.0001$), the medial geniculate (mean T_1 left MGN=1873ms+66ms, mean T_1 right MGN=1813ms+65ms, $p<0.0001$), the lateral posterior nucleus (mean T_1 left LP=1693ms+50ms, mean T_1 right LP=1667ms+47ms, $p=0.0041$), and the pulvinar (mean T_1 left Pu=1758ms+46ms, mean T_1 right Pu=1718ms+47ms, $p<0.0001$).

Significantly longer T_1 values (corrected for multiple comparisons $p<0.0016$) were observed in women compared to men within central-lateral, lateral, lateral-geniculate, medial, medial-geniculate, mediodorsal, posterior, pulvinar, pulvinar-anterior thalamic nuclei, the claustrum, the red-nucleus and the mtt (Table 6).

Table 6: Comparison of T_1 values (Mean+SD in ms) for each hemisphere derived (N=60,Wilcoxon test) and a comparison female and male subjects (N=30, Wilcoxon test), derived from the 7TAMIbrain$_{DGN}$ atlas.

	Names	LH (N=60)	RH (N=60)	Wilcoxon rank test	Female (N=30)	Male (N=30)	Wilcoxon rank test
other deep grey nuclei	Acb	**1917±60**	**2088±76**	**< 0.0001***	2009±116	1996±104	0.52
	Cd	1902±67	1887±48	0.1467	1893±56	1896±61	0.88
	Cl	1619±44	1609±46	0.1675	**1628±40**	**1600±45**	**0.0009***
	Cb	1444±41	1440±41	0.62	1448±43	1436±38	0.13
	GPe	1389±38	1398±40	0.38	1391±35	1396±43	0.56
	GPi	1398±41	1394±42	0.50	1394±37	1399±45	0.72
	Hb	1787±163	1733±78	0.0052	1758±72	1762±170	0.23
	mtt	1495±49	1476±54	0.047	**1504±48**	**1467±50**	**< 0.0001***
	PuT	1691±46	1712±43	0.013	1707±47	1696±44	0.196
	RN	1372±42	1365±43	0.44	**1380±39**	**1357±43**	**0.0015***
	SN	1560±56	1561±56	0.96	1568±59	1553±51	0.15
thalamic nuclei	STh	**1309±41**	**1335±44**	**0.0007***	1330±45	1314±42	0.07
	AV	**1794±57**	**1744±44**	**< 0.0001***	1780±57	1758±54	0.008
	CL	1784±47	1756±46	0.0029	**1786±47**	**1753±44**	**0.0003***
	CM	1631±47	1644±48	0.0137	1648±44	1628±50	0.0135
	LGN	**1533±42**	**1488±41**	**< 0.0001***	**1527±41**	**1494±47**	**0.0005***
	LP	**1693±50**	**1667±47**	**0.0041***	1692±53	1668±44	0.0145
	LT	1542±42	1524±38	0.026	**1549±39**	**1516±36**	**< 0.0001***
	MD	1890±53	1885±46	0.57	**1906±46**	**1868±45**	**< 0.0001***
	MGN	**1873±66**	**1813±65**	**< 0.0001***	**1867±62**	**1819±73**	**0.0012***
	MT	1830±67	1829±60	0.79	**1840±47**	**1819±75**	**0.0014***
	Po	1893±63	1879±66	0.16	**1910±50**	**1862±69**	**< 0.0001***
	Pu	**1758±46**	**1718±47**	**< 0.0001***	**1756±45**	**1719±48**	**< 0.0001***
	PuA	1660±50	1644±48	0.08	**1667±43**	**1636±51**	**0.0002***

* $p<0.05$ corrected for multiple comparisons (for N=60 $p<0.0008$, for N=30 $p<0.0016$).

Correlations between age and T_1 values were significant (post-hoc multiple comparison correction $p<0.0008$) within the claustrum (Rho=-0.339, $p=0.0016$), globus-pallidus-externus (Rho=-0.360, $p=0.0008$), red nuclei (Rho=-

0.436, p<0.0001), sub-thalamic nuclei (Rho=-0.351, p=0.0011), substantia-nigra (Rho=-0.407, p=0.0001) lateral thalami (R=-0.340; p=0.0016), medial thalamic nuclei (Rho=-0.353, p=0.001), mediodorsal thalamic nuclei (Rho=-0.383, p=0.0003) and the MTT (R=-0.430; p<0.0001).

Comparison to T_1 values in the literature

In Table 7 we present the results from four other studies in which T_1 values were estimated for the few DGN in common with our study.

Table 7: Comparison of mean T_1 values (ms) at 7 Tesla in the literature

Nuclei\Study	[Rooney et al., 2007]	[Wright et al., 2008]	[Marques et al., 2010]	[Caan et al., 2019]	Current study
PuT	1700±66	1643±167	1520±90	1630±50	1701±45
Pallidum	1347±52	-	1170±70	-	1395±40
Cd	1745±64	1684±76	1630±90	1800±80	1895±58
RN	-	-	-	1330±70	1369±42
SN	-	-	-	1380±60	1561±56
STh	-	-	-	1280±40	1322±44
Sequence parameters	Look-Locker, 5 mm, one slice, 32 inversion times	MPRAGE, 15 mm, 20 slices, 8 inversion times	MP2RAGE, 0.9 mm, 160 slices	MP2RAGEME, 0.64 mm, 164 slices	MP2RAGE, 0.6mm, 240 slices
number of subjects	3	4	7	8	60

Discussion

We have created a high-resolution consensus-based atlas of DGN and thalamic nuclei built from ultra-high resolution *in vivo* 7T MRI acquisitions, with a corresponding T_1-w template compatible with the MNI space. Coupled with state-of-the-art co-registration procedures, we also provided a set of unbiased quantitative T_1 maps and corresponding T_1 values of DGN derived from sixty young healthy volunteers (30 women / 30 men) that can be used as a control database for clinical research studies conducted in matched populations.

Due to the high spatial resolution and subsequent minimal partial volume effects, the proposed $7TAMIbrain_{T1w\_30}$ template demonstrated enhanced contrast between DGN permitting a straightforward delineation of the small nuclei and the creation of the $7TAMIbrain_{DGN}$ atlas. This was also mainly due to the efficiency of the non-linear registration algorithm SyGN, an unbiased method that accounts for intensity and shape variations allowing fully automatic template derivation and a reduced dependence on anatomical variability, producing an average template with high sharpness. This high-quality template was derived from data of 30 healthy subjects explored at 7T using the MP2RAGE sequence with a nominal resolution of $(0.6mm)^3$. A high contrast template, with a resolution of $0.5mm^2$, was successfully provided by the iterative process improving delineation of structures hardly visible at the individual level.

Though not exhaustive, this atlas integrated some candidates for therapeutic targets in refractory epilepsy [Fisher et al., 2010], refractory pain [Weigel and Krauss, 2004] or major depression [Sartorius et al., 2010] such as the habenula, the anterior and the centromedian thalamic nuclei. The globus pallidus, a potential neurosurgical target in some cases of refractory epilepsy, was also sharply delineated with a good differentiation between the internal and the external parts. The sub-thalamic nucleus (STh), one of the potential target structures in the treatment of advanced PD [Mallet et al., 2008], was also easily characterized as well as the substantia-nigra (SN) also involved in PD and others neurodegenerative disorders such as multiple system atrophy or progressive supranuclear palsy. An additional structure generally poorly characterized by MRI was easily visible on the $7TAMIbrain_{T1w\_30}$ template, i.e. the claustrum, a thin and irregular subcortical grey matter structure located between the external and the extreme capsule, laterally from the putamen and medially from the insula. The fine delineation of the claustrum may contribute to a better understanding of the complex organization of this small structure having numerous projections to visual cortex, frontal and language areas [Torgerson et al., 2015]. The caudate nucleus and the putamen were identified as well as their connecting caudatolenticar bridges. Ventrally to the striatum, the nucleus accumbens was easily delineated [Neto et al., 2008]. Acb is thought to be involved in cognitive, emotional and psychomotor functions, and is therefore one of the possible targets of psychosurgery in obsessive-compulsive and anxiety disorders [Tass et al., 2003].

While the original Morel atlas was derived on postmortem examination of nine stereotactically cut thalamic blocks from five normal human brains and defined in its own space, its electronic version, i.e. the e-Morel atlas [Krauth et al., 2010], has been provided with one T_1-w template in the normalized MNI space. Though the e-Morel atlas cannot be considered as an anatomical 'ground truth' accounting for inter-subject differences, it provides a reliable proxy of thalamic nuclei location in an individual subject after co-registration. To limit this uncertainty, the present 7TAMIbrain$_{DGN}$ atlas was based on a manual segmentation procedure with delineation of visible boundaries only. Our atlas was somewhat different from the 'adapted e-Morel' atlas (with the same number of parcels per hemisphere) as shown by the DSC and the differences in mean T_1 values of thalamic nuclei. Interestingly, the largest differences were obtained for structures at the interface of CSF or large white matter bundles with lower variance for regions in our atlas. This suggests greater homogeneity of regions with less partial volume effects in the 7TAMIbrain$_{DGN}$ atlas, or improved accuracy of T_1 measurements using the proposed methodology.

Though time consuming – especially with such ultrahigh resolution images – manual segmentation is considered the gold standard and the majority of automated segmentations are still calibrated by reference to expert manual segmentations [Patenaude et al., 2011]. The delineation of the parcels has been shown to be robust to the individual registration of the atlas onto individual subject space (Fig6). Again, the choice of the nonlinear registration SyN approach was driven by previous reports showing better results with non-linear versus other registration techniques [Chakravarty et al., 2009], and more precisely, the superiority of SyN out of fourteen nonlinear algorithms [Klein et al., 2009]. This automatic approach may also be more time-efficient without loss of performance compared to the Automatic Nonlinear Image Matching and Anatomical Labeling (ANIMAL) registration for the segmentation of deep brain structures in patients with PD [Haegelen et al., 2013], and simpler to implement than less time-consuming techniques such as the patch-based fusion technique [Coupe et al., 2011] which requires the supervision of an expert engineer. Here, some sub-structures such as the globus-pallidus-internus or thalamic nuclei, though poorly defined on individual T_1-w or T1map images (Fig6), were successfully assigned in individuals thanks to the SyN registrations on the 7TAMIbrain$_{T1w_30}$ template and the corresponding 7TAMIbrain$_{DGN}$ atlas.

It is worth noting that when using the present template, twelve out of the thirty-one thalamic nuclei were directly segmented based on visual contrast only. This strategy should contribute to improved alignment of individual subjects according to well-observed borders within thalami, adding a more relevant prior than external thalamic contours only or a few visible landmarks. For example, the weak contrast of the template associated with the e-Morel atlas questions the precision of the localization of the boundaries of these nuclei. Our approach improves this localization by an optimal registration process greatly improved by the contrast and the native resolution of our template. Further gains in the spatial resolution of the reconstructed template are possible with a higher number of subjects. Probabilistic atlases based on *ex-vivo* MRI and histological data indicate a greater number of thalamic sub-nuclei but without the clear definition certain boundaries being in individual data, thus limiting coregistration processes [Iglesias et al., 2018]. Optimized contrasts such as white matter nulled 3D-MPRAGE have been shown to improve automatic parcellation of thalamic nuclei using multi-atlas approaches (THOMAS [Su et al., 2019]) but did not included the entire thalamus volume when adding labels and required a special acquisition used for this specific purpose (i.e. WM-nulled MP-RAGE [Tourdias et al., 2014][Saranathan et al., 2015]). For example, regions not included in the thalamic atlases of FSL, Freesurfer and THOMAS such as the central lateral thalamic nuclei located in the internal medullary lamina of the thalamus were easily depicted on the 7TAMIbrain$_{T1w_30}$ template with hyperintense signal on the T_1-w image due to high myelin content. The present 7TAMIbrain$_{DGN}$ atlas was created from an ultra-high-resolution template using native MP2RAGE sequence which is the gold standard for anatomical exploration at 7T. Nevertheless, some DGN identified on histological data with specific cytoarchitectonic and myeloarchitectonic features [Jones, E.G., 2007; Morel, 2007], or using connectivity-based segmentation with probabilistic tractography [Draganski et al., 2008] were too small/poorly defined to be accurately identified on our 7TAMIbrain$_{T1w_30}$ template. Diffusion MRI has provided relevant thalamic connectivity based parcellation [Behrens et al., 2003], permitting the localization in individuals of relevant small targets such as the ventral intermediate nucleus (VIM) based on thalamo-cerebellar connectivity [Akram et al., 2018]. The use of mixed approaches combining anatomical atlases with well-defined visible boundaries and functional connectivity clustering has contributed to better characterizing the organization of precise networks such as the basal ganglia-thalamocortical loop in tonic-clonic seizures [He et al., 2020]. Through common references and terminology for thalamic nuclei [Mai and Majtanik, 2019] combination of multiple atlases derived from various approaches should provide a more adaptative process at the individual level, such as combining submillimetric anatomical multicontrast atlases that have well-defined boundaries (including T_1-w, T_2*w, T_1 maps and QSM) and structural and functional connectivity derived parcellation of groups of thalamic nuclei that are not well defined anatomically.

The MP2RAGE data used to construct the 7TAMIbrain$_{T1w_30}$ template also provided access to corresponding quantitative T_1 maps with low standard deviation within the studied structures. The DGN T_1 values obtained were in

good agreement with those reported in the literature at 7 Tesla (Table 7). The MP2RAGE sequence was chosen both for the high resolution and robustness of T_1 values, which are independent of the receive magnetic field, M_0 and T_2* despite the presence of significant RF field inhomogeneities at 7T [Marques and Gruetter, 2013]. In this study, special attention has been paid to correct for residual sensitivity to B_1^+ inhomogeneities affecting the T_1 maps, by accounting for B_1^+ variation in the unbiased T_1 estimation process. These high-quality and unbiased T_1 maps obtained in a cohort of sixty young healthy subjects (mean age 24 [19-45]) revealed differences in tissue organization and microstructure between the different DGN and thalamic nuclei, but also differences according to sex, age and brain hemisphere. Such variations in T_1 values may be due to differences in the anatomical arrangement of fibers in each nucleus, modifying the distribution of free water and macromolecules and so influencing T_1 relaxation, in addition to other physiological mechanisms related to iron deposition or the extent of myelination. For example, myelin density and maturation tend to decrease T_1 values in line with the observed negative correlation of T_1 values with age in this control population at the end of adolescence and early adulthood in myelinated structures such as medial thalamic nuclei, mediodorsal thalamic nuclei and the mtt. Other physiological phenomena can lead to decreased T_1 in tissue. Different DGN have previously been shown to have significant differences in T_1 and T_2 values between the major nuclei groups [Deoni et al., 2005], which could be used to perform partial automatic segmentation using a k-means clustering algorithm [Deoni et al., 2008] or multi-contrast segmentation [Traynor et al., 2011]. Divergent T_1 values have been observed between different small regions of interest positioned within 15 thalamic nuclei using an optimized MPRAGE sequence at 7T [Tourdias et al., 2014]. In the present study we also observed significant negative correlation between T_1 values and age in DGN regions known to be prone to iron deposit during normal aging or neurodegenerative diseases such as red nuclei, sub-thalamic nuclei or the substantia-nigra [Saha et al., 2013].

Concerning gender, functional connectomes have shown differences between female and male subjects with differences in connectivity topology reflected by different hub rankings and weightings of edges linking bilateral thalami and the left thalamus to ipsilateral precentral cortex and hippocampus [Andjelković et al., 2020]. Involvement of the thalamus in reward and loss processes appears to differ in male and female subjects [Zhang et al., 2020]. Such functional differences should be accompanied by structural differences within hubs. As an example, differences in ferritin iron levels between women and men have been observed in the thalamus and in the caudate, another important hub [Bartzokis et al., 2007]. Structural characteristics (FA and volume) of the left thalamus specifically has been identified as one of the highest contributors for deep learning classification accuracy when discriminating female and male brains, highlighting both differences in structure and differences between hemispheres [Xin et al., 2019]. In line with this, few studies have reported on the differences in signal intensities between hemispheres. Iron content evaluated by T_2* [Haacke et al., 2010] or QSM [Lim et al., 2013] appear to vary between hemispheres in some nuclei such as the pulvinar and putamen. Similarly, White et al. found a higher signal ratio in the left pulvinar compared to the right on T_2-weighted images, and the opposite for the globus-pallidus [White et al., 2014]. A recent study has shown metabolite differences in each thalamic nuclei and between hemispheres using ^{1}H-magnetic resonance spectroscopy that could be explained by cellular, functional and structural differences [Donadieu et al., 2016].

The main limitation of the study was related to the fact that, given the very high number of slices to process, only two expert operators have performed the manual segmentation. This procedure might be subject to errors of delineation, as well as to the subjective character of this segmentation task. Nevertheless, in addition to a third neuroradiologist who validated the segmentation, the high-resolution atlas was applied to all subjects without requiring any post-hoc correction by the three experts, demonstrating the robustness of the non-linear registration procedure and of the atlas. Post-processing was time-consuming for clinical usage (several hours for one subject) but optimization could speed up the process with computation of the non-linear registration applied to the DGN region only instead of the entire brain. Comparison with CIT168 atlas and an adapted e-Morel atlas (modified for comparable parcellation) showed the relevance of the proposed DGN and thalamic segmentation, which is subject to lower partial volume effects, consistent with lower variance of T_1 values within parcels and lower T_1 values in small regions such as the habenula. The characterized population in the present study is young, and as such should not be used as control database for aged patients.

Conclusion

We have proposed 7TAMIbrain, a validated database including one ultra-high-resolution T_1w MR average template of the whole brain ($7TAMIbrain_{T1w\_30}$), one atlas of deep grey matter nuclei ($7TAMIbrain_{DGN}$) and a set of sixty individual unbiased volumetric T_1 maps ($SUBJECT_{qT1}$) derived from and applicable to MP2RAGE images to locate and characterize the principal brain deep grey matter structures. This robust database of quantitative T_1 values of DGN provides the basis for individual level characterization of the extent of tissue microstructural damage in patients with neurological diseases affecting the DGN and in particular the thalamic nuclei.

Data/code availability statement

The full 7TAMIbrain [Girard et al., 2021] dataset (BIDS formatted) is publicly available on the OpenNeuro platform (Dataset ds003967). Source code for T1 bias correction and script for registration can be found at: https://github.com/arnaudletroter/7TAMIBrain

Acknowledgments

The authors thank Dr Tobias Kober (Siemens Healthcare) for helpful discussions about the T_1 mapping methodology with the MP2RAGE sequence. The authors thank Prof. Dr. Van Gool (Computer Vision Laboratory, ETH Zürich) for providing access to the electronic Morel Atlas. The project leading to this publication has received funding from Excellence Initiative of Aix-Marseille University - A*MIDEX, a French "Investissements d'Avenir" programme through the 7T-AMISTART program (E&I 2013). This work was performed on the platform 7T-AMI, a French "Investissements d'Avenir programme" (grant ANR-11-EQPX-0001). This work was performed by a laboratory member of the France Life Imaging network (grant ANR-11-INBS-0006) and the **Neuromarseille Institute** (A*MIDEX).

Author Contributions

All authors contributed scientifically to this paper.
G.B., A.L.T., P.B., A.M., L.D.R., O.M.G., B.R., M.G., J.P.R. contributed to drafting and revising the article
G.B., A.L.T., P.B., M.G., J.P.R., contributed to the conception and the design of the experiments.
G.B., B.T, A.L.T., L.D.R, O.M.G., P.B., A.M., B.R., M.G., J.P.R. contributed to the collection, analysis and interpretation of the data.
A.L.T., O.M.G., L.D.R, A.M., P.B. developed the post-processing pipeline. G.B., A.L.T., J.P.R. prepared the figures.
G.B., B.T., P.L., N.G., M.G. performed clinical interpretations.

Competing interests

The author(s) declare no competing interests.

Abbreviations

ac: anterior commissure
Acb: accumbens
al: ansa lenticularis
AV: anterior
bAVD: Balanced average Hausdorff distance
Cd: caudate
CI: claustrum
CL: central-lateral
Cb: caudatolenticar bridges
CM: centromedian
DGN: Deep Grey matter Nuclei
DSC: Dice Similarity Coefficient
eC: external capsule
eml: external medullary lamina
EXA: extended-amygdala
ExC: extreme capsule
fct: fasciculus cerebellothalamicus
fl: fasciculus lenticularis
ft: fasciculus thalamicus
fx: fornix
GPe: globus-pallidus-externus
GPi: globus-pallidus-internus
Hb: habenula
HTH: hypothalamus
ial: internal accessory lamina
iC: internal capsule
Ic: inferior colliculus
iml: internal medullary lamina
LGN: lateral-geniculate
LP: lateral-posterior
LT: lateral
MD: mediodorsal
MGN: medial-geniculate
ml: medial lemniscus
MN: mammillary-nucleus
MT: medial
mtt: mammillothalamic tract
ot: optic tract
pc: posterior commissure
PAG: periaqueductal grey area
PBP: parabrachial-pigmented-nucleus
PD: Parkinson's disease
Po: posterior
Pu: pulvinar
PuA: pulvinar-anterior
PuT: putamen
RN: red-nucleus
Sc: superior colliculus
SN: substantia-nigra
STh: sub-thalamic
stt: spinothalamic tract
V3: third ventricle
VeP: ventral-pallidum
VIM: ventral intermediate nucleus
VOLSMTY: Volumetric Similarity Index
VTA: ventral-tegmental-area
ZI: zona incerta

References

Abosch A, Yacoub E, Ugurbil K, Harel N (2010): An assessment of current brain targets for deep brain stimulation surgery with susceptibility-weighted imaging at 7 tesla. Neurosurgery 67:1745–1756; discussion 1756.

Akram H, Dayal V, Mahlknecht P, Georgiev D, Hyam J, Foltynie T, Limousin P, De Vita E, Jahanshahi M, Ashburner J, Behrens T, Hariz M, Zrinzo L (2018): Connectivity derived thalamic segmentation in deep brain stimulation for tremor. NeuroImage: Clinical 18:130–142.

Andjelković M, Tadić B, Melnik R (2020): The topology of higher-order complexes associated with brain hubs in human connectomes. Sci Rep 10:17320.

Avants BB, Epstein CL, Grossman M, Gee JC (2008): Symmetric diffeomorphic image registration with cross-correlation: evaluating automated labeling of elderly and neurodegenerative brain. Med Image Anal 12:26–41.

Avants BB, Tustison NJ, Song G, Cook PA, Klein A, Gee JC (2011): A reproducible evaluation of ANTs similarity metric performance in brain image registration. Neuroimage 54:2033–2044.

Avants BB, Yushkevich P, Pluta J, Minkoff D, Korczykowski M, Detre J, Gee JC (2010): The optimal template effect in hippocampus studies of diseased populations. Neuroimage 49:2457–2466.

Aydin OU, Taha AA, Hilbert A, Khalil AA, Galinovic I, Fiebach JB, Frey D, Madai VI (2021): On the usage of average Hausdorff distance for segmentation performance assessment: hidden error when used for ranking. Eur Radiol Exp 5:4.

Bartzokis G, Tishler TA, Lu PH, Villablanca P, Altshuler LL, Carter M, Huang D, Edwards N, Mintz J (2007): Brain ferritin iron may influence age- and gender-related risks of neurodegeneration. Neurobiol Aging 28:414–423.

Battistella G, Najdenovska E, Maeder P, Ghazaleh N, Daducci A, Thiran J-P, Jacquemont S, Tuleasca C, Levivier M, Bach Cuadra M, Fornari E (2017): Robust thalamic nuclei segmentation method based on local diffusion magnetic resonance properties. Brain Struct Funct 222:2203–2216.

Bazin P-L, Pham DL (2008): Homeomorphic brain image segmentation with topological and statistical atlases. Med Image Anal 12:616–625.

Behrens TEJ, Johansen-Berg H, Woolrich MW, Smith SM, Wheeler-Kingshott CAM, Boulby PA, Barker GJ, Sillery EL, Sheehan K, Ciccarelli O, Thompson AJ, Brady JM, Matthews PM (2003): Non-invasive mapping of connections between human thalamus and cortex using diffusion imaging. Nat Neurosci 6:750–757.

Bender B, Manz C, Korn A, Nagele T, Klose U (2011): Optimized 3D magnetization-prepared rapid acquisition of gradient echo: identification of thalamus substructures at 3T. AJNR Am J Neuroradiol 32:2110–2115.

Bonnier G, Kober T, Schluep M, Du Pasquier R, Krueger G, Meuli R, Granziera C, Roche A (2016): A New Approach for Deep Gray Matter Analysis Using Partial-Volume Estimation. PLoS One 11:e0148631.

Caan MWA, Bazin P, Marques JP, Hollander G, Dumoulin SO, Zwaag W (2019): MP2RAGEME: T_1, T_2^*, and QSM mapping in one sequence at 7 tesla. Hum Brain Mapp 40:1786–1798.

Calamante F, Oh S-H, Tournier J-D, Park S-Y, Son Y-D, Chung J-Y, Chi J-G, Jackson GD, Park C-W, Kim Y-B, Connelly A, Cho Z-H (2013): Super-resolution track-density imaging of thalamic substructures: comparison with high-resolution anatomical magnetic resonance imaging at 7.0T. Hum Brain Mapp 34:2538–2548.

Chakravarty MM, Bertrand G, Hodge CP, Sadikot AF, Collins DL (2006): The creation of a brain atlas for image guided neurosurgery using serial histological data. Neuroimage 30:359–376.

Chakravarty MM, Sadikot AF, Germann J, Hellier P, Bertrand G, Collins DL (2009): Comparison of piece-wise linear, linear, and nonlinear atlas-to-patient warping techniques: analysis of the labeling of subcortical nuclei for functional neurosurgical applications. Hum Brain Mapp 30:3574–3595.

Corona V, Lellmann J, Nestor P, Schönlieb C-B, Acosta-Cabronero J (2019): A multi-contrast MRI approach to thalamus segmentation:17.

Coupe P, Manjon JV, Fonov V, Pruessner J, Robles M, Collins DL (2011): Patch-based segmentation using expert priors: application to hippocampus and ventricle segmentation. Neuroimage 54:940–954.

Datta R, Bacchus MK, Kumar D, Elliott MA, Rao A, Dolui S, Reddy R, Banwell BL, Saranathan M (2020): Fast automatic segmentation of thalamic nuclei from MP2RAGE acquisition at 7 Tesla. Magn Reson Med:mrm.28608.

Deistung A, Schafer A, Schweser F, Biedermann U, Turner R, Reichenbach JR (2013): Toward in vivo histology: a comparison of quantitative susceptibility mapping (QSM) with magnitude-, phase-, and R2*-imaging at ultra-high magnetic field strength. Neuroimage 65:299–314.

Deoni SCL, Josseau MJC, Rutt BK, Peters TM (2005): Visualization of thalamic nuclei on high resolution, multi-averaged T1 and T2 maps acquired at 1.5 T. Hum Brain Mapp 25:353–359.

Deoni SCL, Williams SCR, Jezzard P, Suckling J, Murphy DGM, Jones DK (2008): Standardized structural magnetic resonance imaging in multicentre studies using quantitative T1 and T2 imaging at 1.5 T. Neuroimage 40:662–671.

Donadieu M, Le Fur Y, Confort-Gouny S, Le Troter A, Guye M, Ranjeva J-P (2016): Evidencing different

neurochemical profiles between thalamic nuclei using high resolution 2D-PRESS semi-LASER (1)H-MRSI at 7 T. MAGMA 29:491–501.
Draganski B, Kherif F, Kloppel S, Cook PA, Alexander DC, Parker GJM, Deichmann R, Ashburner J, Frackowiak RSJ (2008): Evidence for Segregated and Integrative Connectivity Patterns in the Human Basal Ganglia. Journal of Neuroscience 28:7143–7152.
Eapen M, Zald DH, Gatenby JC, Ding Z, Gore JC (2011): Using high-resolution MR imaging at 7T to evaluate the anatomy of the midbrain dopaminergic system. AJNR Am J Neuroradiol 32:688–694.
Federau C, Gallichan D (2016): Motion-Correction Enabled Ultra-High Resolution In-Vivo 7T-MRI of the Brain. PLoS One 11:e0154974.
Fisher R, Salanova V, Witt T, Worth R, Henry T, Gross R, Oommen K, Osorio I, Nazzaro J, Labar D, Kaplitt M, Sperling M, Sandok E, Neal J, Handforth A, Stern J, DeSalles A, Chung S, Shetter A, Bergen D, Bakay R, Henderson J, French J, Baltuch G, Rosenfeld W, Youkilis A, Marks W, Garcia P, Barbaro N, Fountain N, Bazil C, Goodman R, McKhann G, Babu Krishnamurthy K, Papavassiliou S, Epstein C, Pollard J, Tonder L, Grebin J, Coffey R, Graves N (2010): Electrical stimulation of the anterior nucleus of thalamus for treatment of refractory epilepsy. Epilepsia 51:899–908.
Fonov V, Evans A, McKinstry R, Almli C, Collins D (2009): Unbiased nonlinear average age-appropriate brain templates from birth to adulthood. NeuroImage 47:S102.
Girard O, De Rochefort L, Guye M, Ranjeva J-P, Le Troter A (2021): 7TAMIbrain. Openneuro. https://openneuro.org/datasets/ds003967/versions/1.0.0.
Gringel T, Schulz-Schaeffer W, Elolf E, Frolich A, Dechent P, Helms G (2009): Optimized high-resolution mapping of magnetization transfer (MT) at 3 Tesla for direct visualization of substructures of the human thalamus in clinically feasible measurement time. J Magn Reson Imaging 29:1285–1292.
Haacke EM, Miao Y, Liu M, Habib CA, Katkuri Y, Liu T, Yang Z, Lang Z, Hu J, Wu J (2010): Correlation of putative iron content as represented by changes in R2* and phase with age in deep gray matter of healthy adults. J Magn Reson Imaging 32:561–576.
Haegelen C, Coupe P, Fonov V, Guizard N, Jannin P, Morandi X, Collins DL (2013): Automated segmentation of basal ganglia and deep brain structures in MRI of Parkinson's disease. Int J Comput Assist Radiol Surg 8:99–110.
He X, Chaitanya G, Asma B, Caciagli L, Bassett DS, Tracy JI, Sperling MR (2020): Disrupted basal ganglia–thalamocortical loops in focal to bilateral tonic-clonic seizures. Basal ganglia 143:Page e24.
Hwang K, Bertolero MA, Liu WB, D'Esposito M (2017): The Human Thalamus Is an Integrative Hub for Functional Brain Networks. J Neurosci 37:5594–5607.
Ide S, Kakeda S, Korogi Y (2015): [Anatomy of the Thalamus]. Brain Nerve 67:1459–1469.
Iglesias JE, Insausti R, Lerma-Usabiaga G, Bocchetta M, Van Leemput K, Greve DN, van der Kouwe A, Alzheimer's Disease Neuroimaging Initiative, Fischl B, Caballero-Gaudes C, Paz-Alonso PM (2018): A probabilistic atlas of the human thalamic nuclei combining ex vivo MRI and histology. Neuroimage 183:314–326.
Jakab A, Blanc R, Berényi EL, Székely G (2012): Generation of Individualized Thalamus Target Maps by Using Statistical Shape Models and Thalamocortical Tractography. AJNR Am J Neuroradiol 33:2110–2116.
Johansen-Berg H, Behrens TEJ, Sillery E, Ciccarelli O, Thompson AJ, Smith SM, Matthews PM (2005): Functional-anatomical validation and individual variation of diffusion tractography-based segmentation of the human thalamus. Cereb Cortex 15:31–39.
Jones, E.G. (2007): The Thalamus. Vol. 326.
Klein A, Andersson J, Ardekani BA, Ashburner J, Avants B, Chiang M-C, Christensen GE, Collins DL, Gee J, Hellier P, Song JH, Jenkinson M, Lepage C, Rueckert D, Thompson P, Vercauteren T, Woods RP, Mann JJ, Parsey RV (2009): Evaluation of 14 nonlinear deformation algorithms applied to human brain MRI registration. Neuroimage 46:786–802.
Krauth A, Blanc R, Poveda A, Jeanmonod D, Morel A, Szekely G (2010): A mean three-dimensional atlas of the human thalamus: generation from multiple histological data. Neuroimage 49:2053–2062.
Lambert C, Simon H, Colman J, Barrick TR (2017): Defining thalamic nuclei and topographic connectivity gradients in vivo. Neuroimage 158:466–479.
Lau JC, Xiao Y, Haast RAM, Gilmore G, Uludağ K, MacDougall KW, Menon RS, Parrent AG, Peters TM, Khan AR (2020): Direct visualization and characterization of the human zona incerta and surrounding structures. Hum Brain Mapp 41:4500–4517.
Lemaire J-J, Sakka L, Ouchchane L, Caire F, Gabrillargues J, Bonny J-M (2010): Anatomy of the human thalamus based on spontaneous contrast and microscopic voxels in high-field magnetic resonance imaging. Neurosurgery 66:161–172.
Lenglet C, Abosch A, Yacoub E, De Martino F, Sapiro G, Harel N (2012): Comprehensive in vivo mapping of the human basal ganglia and thalamic connectome in individuals using 7T MRI. PLoS One 7:e29153.

Lim IAL, Faria AV, Li X, Hsu JTC, Airan RD, Mori S, van Zijl PCM (2013): Human brain atlas for automated region of interest selection in quantitative susceptibility mapping: application to determine iron content in deep gray matter structures. Neuroimage 82:449–469.
Magnotta VA, Gold S, Andreasen NC, Ehrhardt JC, Yuh WT (2000): Visualization of subthalamic nuclei with cortex attenuated inversion recovery MR imaging. Neuroimage 11:341–346.
Mai JK, Majtanik M (2019): Toward a Common Terminology for the Thalamus. Front Neuroanat 12:114.
Mallet L, Polosan M, Jaafari N, Baup N, Welter M-L, Fontaine D, du Montcel ST, Yelnik J, Chereau I, Arbus C, Raoul S, Aouizerate B, Damier P, Chabardes S, Czernecki V, Ardouin C, Krebs M-O, Bardinet E, Chaynes P, Burbaud P, Cornu P, Derost P, Bougerol T, Bataille B, Mattei V, Dormont D, Devaux B, Verin M, Houeto J-L, Pollak P, Benabid A-L, Agid Y, Krack P, Millet B, Pelissolo A (2008): Subthalamic nucleus stimulation in severe obsessive-compulsive disorder. N Engl J Med 359:2121–2134.
Marques JP, Gruetter R (2013): New developments and applications of the MP2RAGE sequence--focusing the contrast and high spatial resolution R1 mapping. PLoS One 8:e69294.
Marques JP, Kober T, Krueger G, van der Zwaag W, Van de Moortele P-F, Gruetter R (2010): MP2RAGE, a self bias-field corrected sequence for improved segmentation and. Neuroimage 49:1271–1281.
Massire A, Taso M, Besson P, Guye M, Ranjeva J-P, Callot V (2016): High-resolution multi-parametric quantitative magnetic resonance imaging of the human cervical spinal cord at 7T. Neuroimage 143:58–69.
McCarthy, Paul (2020): FSLeyes. Zenodo. https://zenodo.org/record/3858136.
Morel A, Magnin M, Jeanmonod D (1997): Multiarchitectonic and stereotactic atlas of the human thalamus. J Comp Neurol 387:588–630.
Morel A (2007): Stereotactic Atlas of the Human Thalamus and Basal Ganglia. CRC Press. https://books.google.fr/books?hl=fr&lr=&id=b9m3dlu2kX4C&oi=fnd&pg=PP1&ots=-1oMenmTXg&sig=gRFbVEznK_RfUrJZ_Rr-GIE_mqA&redir_esc=y#v=onepage&q&f=false.
Najdenovska E, Tuleasca C, Jorge J, Maeder P, Marques JP, Roine T, Gallichan D, Thiran J-P, Levivier M, Bach Cuadra M (2019): Comparison of MRI-based automated segmentation methods and functional neurosurgery targeting with direct visualization of the Ventro-intermediate thalamic nucleus at 7T. Sci Rep 9:1119.
Neto LL, Oliveira E, Correia F, Ferreira AG (2008): The human nucleus accumbens: where is it? A stereotactic, anatomical and magnetic resonance imaging study. Neuromodulation 11:13–22.
Neudorfer C, Germann J, Elias GJB, Gramer R, Boutet A, Lozano AM (2020): A high-resolution in vivo magnetic resonance imaging atlas of the human hypothalamic region. Sci Data 7:305.
Niemann K, Mennicken VR, Jeanmonod D, Morel A (2000): The Morel stereotactic atlas of the human thalamus: atlas-to-MR registration of internally consistent canonical model. Neuroimage 12:601–616.
Nowogrodzki A (2018): The world's strongest MRI machines are pushing human imaging to new limits. Nature 563:24–26.
Patenaude B, Smith SM, Kennedy DN, Jenkinson M (2011): A Bayesian model of shape and appearance for subcortical brain segmentation. Neuroimage 56:907–922.
Pauli WM, Nili AN, Tyszka JM (2018): A high-resolution probabilistic in vivo atlas of human subcortical brain nuclei. Sci Data 5:180063.
Planche V, Su JH, Mournet S, Saranathan M, Dousset V, Han M, Rutt BK, Tourdias T (2019): White-matter-nulled MPRAGE at 7T reveals thalamic lesions and atrophy of specific thalamic nuclei in multiple sclerosis. Mult Scler:1352458519828297.
Rohlfing T, Maurer CR (2007): Shape-Based Averaging. IEEE Trans on Image Process 16:153–161.
Rooney WD, Johnson G, Li X, Cohen ER, Kim S-G, Ugurbil K, Springer CS (2007): Magnetic field and tissue dependencies of human brain longitudinal 1H2O relaxation in vivo. Magn Reson Med 57:308–318.
Saha P, Andia ME, Modarai B, Blume U, Humphries J, Patel AS, Phinikaridou A, Evans CE, Mattock K, Grover SP, Ahmad A, Lyons OT, Attia RQ, Renne T, Premaratne S, Wiethoff AJ, Botnar RM, Schaeffter T, Waltham M, Smith A (2013): Magnetic resonance T1 relaxation time of venous thrombus is determined by iron processing and predicts susceptibility to lysis. Circulation 128:729–736.
Saranathan M, Tourdias T, Bayram E, Ghanouni P, Rutt BK (2015): Optimization of white-matter-nulled magnetization prepared rapid gradient echo (MP-RAGE) imaging: Optimization of White-Matter-Nulled MP-RAGE Imaging. Magn Reson Med 73:1786–1794.
Sartorius A, Kiening KL, Kirsch P, von Gall CC, Haberkorn U, Unterberg AW, Henn FA, Meyer-Lindenberg A (2010): Remission of major depression under deep brain stimulation of the lateral habenula in a therapy-refractory patient. Biol Psychiatry 67:e9–e11.
Su JH, Thomas FT, Kasoff WS, Tourdias T, Choi EY, Rutt BK, Saranathan M (2019): Thalamus Optimized Multi Atlas Segmentation (THOMAS): fast, fully automated segmentation of thalamic nuclei from structural MRI.

Neuroimage 194:272–282.
Sudhyadhom A, Haq IU, Foote KD, Okun MS, Bova FJ (2009): A high resolution and high contrast MRI for differentiation of subcortical structures for DBS targeting: the Fast Gray Matter Acquisition T1 Inversion Recovery (FGATIR). Neuroimage 47 Suppl 2:T44-52.
Taha AA, Hanbury A (2015): Metrics for evaluating 3D medical image segmentation: analysis, selection, and tool. BMC Med Imaging 15:29.
Talairach, J. (1957): Atlas d'anatomie stéréotaxique: repérage radiologique indirect des noyaux gris centraux des régions mésencéphalo-sous-optique et hypothalamique de l'homme. Masson.
Tass PA, Klosterkotter J, Schneider F, Lenartz D, Koulousakis A, Sturm V (2003): Obsessive-compulsive disorder: development of demand-controlled deep brain stimulation with methods from stochastic phase resetting. Neuropsychopharmacology 28 Suppl 1:S27-34.
Toga AW, Thompson PM, Mori S, Amunts K, Zilles K (2006): Towards multimodal atlases of the human brain. Nat Rev Neurosci 7:952–966.
Torgerson CM, Irimia A, Goh SYM, Van Horn JD (2015): The DTI connectivity of the human claustrum. Hum Brain Mapp 36:827–838.
Tourdias T, Saranathan M, Levesque IR, Su J, Rutt BK (2014): Visualization of intra-thalamic nuclei with optimized white-matter-nulled MPRAGE at 7T. Neuroimage 84:534–545.
Traynor C, Heckemann RA, Hammers A, O'Muircheartaigh J, Crum WR, Barker GJ, Richardson MP (2010): Reproducibility of thalamic segmentation based on probabilistic tractography. Neuroimage 52:69–85.
Traynor CR, Barker GJ, Crum WR, Williams SCR, Richardson MP (2011): Segmentation of the thalamus in MRI based on T1 and T2. Neuroimage 56:939–950.
Tyszka JM, Pauli WM (2016): In vivo delineation of subdivisions of the human amygdaloid complex in a high-resolution group template: In Vivo Amygdala Subdivisions. Hum Brain Mapp 37:3979–3998.
Weigel R, Krauss JK (2004): Center median-parafascicular complex and pain control. Review from a neurosurgical perspective. Stereotact Funct Neurosurg 82:115–126.
White ML, Zhang Y, Helvey JT, Yu F, Omojola MF (2014): Effects of Age, Gender and Hemispheric Location on T2 Hypointensity in the Pulvinar at 3T. Neuroradiol J 27:645–652.
Wiegell MR, Tuch DS, Larsson HBW, Wedeen VJ (2003): Automatic segmentation of thalamic nuclei from diffusion tensor magnetic resonance imaging. Neuroimage 19:391–401.
Wright PJ, Mougin OE, Totman JJ, Peters AM, Brookes MJ, Coxon R, Morris PE, Clemence M, Francis ST, Bowtell RW, Gowland PA (2008): Water proton T1 measurements in brain tissue at 7, 3, and 1.5 T using IR-EPI, IR-TSE, and MPRAGE: results and optimization. MAGMA 21:121–130.
Xin J, Zhang Y, Tang Y, Yang Y (2019): Brain Differences Between Men and Women: Evidence From Deep Learning. Front Neurosci 13:185.
Yang C, Wang Q, Wu W, Xue Y, Lu W, Wu S (2015): Thalamic segmentation based on improved fuzzy connectedness in structural MRI. Comput Biol Med 66:222–234.
Yelnik J, Bardinet E, Dormont D, Malandain G, Ourselin S, Tande D, Karachi C, Ayache N, Cornu P, Agid Y (2007): A three-dimensional, histological and deformable atlas of the human basal ganglia. I. Atlas construction based on immunohistochemical and MRI data. Neuroimage 34:618–638.
Zeineh MM, Parekh MB, Zaharchuk G, Su JH, Rosenberg J, Fischbein NJ, Rutt BK (2014): Ultrahigh-resolution imaging of the human brain with phase-cycled balanced steady-state free precession at 7 T. Invest Radiol 49:278–289.
Zhang J, Hu Y, Wang Z, Wang M, Dong G-H (2020): Males are more sensitive to reward and less sensitive to loss than females among people with internet gaming disorder: fMRI evidence from a card-guessing task. BMC Psychiatry 20:357.